2018

MAGNETO-OPTICAL PROPERTIES OF THIN PERMALLOY FILMS: A STUDY OF THE MAGNETO-OPTICAL GENERATION OF LIGHT CARRYING ANGULAR MOMENTUM

Patrick D. Montgomery
University of Kentucky, pdmo222@uky.edu
Digital Object Identifier: https://doi.org/10.13023/etd.2018.461

STUDENT AGREEMENT:

I represent that my thesis or dissertation and abstract are my original work. Proper attribution has been given to all outside sources. I understand that I am solely responsible for obtaining any needed copyright permissions. I have obtained needed written permission statement(s) from the owner(s) of each third-party copyrighted matter to be included in my work, allowing electronic distribution (if such use is not permitted by the fair use doctrine) which will be submitted to UKnowledge as Additional File.

I hereby grant to The University of Kentucky and its agents the irrevocable, non-exclusive, and royalty-free license to archive and make accessible my work in whole or in part in all forms of media, now or hereafter known. I agree that the document mentioned above may be made available immediately for worldwide access unless an embargo applies.

I retain all other ownership rights to the copyright of my work. I also retain the right to use in future works (such as articles or books) all or part of my work. I understand that I am free to register the copyright to my work.

REVIEW, APPROVAL AND ACCEPTANCE

The document mentioned above has been reviewed and accepted by the student's advisor, on behalf of the advisory committee, and by the Director of Graduate Studies (DGS), on behalf of the program; we verify that this is the final, approved version of the student's thesis including all changes required by the advisory committee. The undersigned agree to abide by the statements above.

Patrick D. Montgomery, Student

Dr. J. Todd Hastings, Major Professor

Dr. Aaron Cramer, Director of Graduate Studies

MAGNETO-OPTICAL PROPERTIES OF THIN PERMALLOY FILMS: A STUDY OF THE MAGNETO-OPTICAL GENERATION OF LIGHT CARRYING ANGULAR MOMENTUM

THESIS

A thesis submitted in partial fulfillment of the requirements for the degree of Master of Science in Electrical Engineering in the College of Engineering at the University of Kentucky

By: Patrick D. Montgomery

Lexington, Kentucky

Director: Dr. J. Todd Hastings, Professor of Electrical Engineering

Lexington, Kentucky

2018

ABSTRACT OF THESIS

MAGNETO-OPTICAL PROPERTIES OF THIN PERMALLOY FILMS: A STUDY OF THE MAGNETO-OPTICAL GENERATION OF LIGHT CARRYING ANGULAR MOMENTUM

Magneto-optical materials such as permalloy can be used to create artificial spin-ice (ASI) lattices with antiferromagnetic ordering. Magneto-optical materials used to create diffraction lattices are known to exhibit magnetic scattering at the half-order Bragg peak while in the ground state. The significant drawbacks of studying the magneto-optical generation of OAM using x-rays are cost, time, and access to proper equipment. In this work, it is shown that the possibility of studying OAM and magneto-optical materials in the spectrum of visible light at or around 2 eV is viable. Using spectroscopic ellipsometry it is possible to detect a change in the magnetization of thin permalloy films with thicknesses between 5 and 20 nm. Patterns consistent with OAM were found at 1.95 eV using a square lattice with a 4π radial phase shift in the antiferromagnetic ground state. Evidence of magnetic scattering at the half-order Bragg peak using 1.95 eV was also found.

KEYWORDS: Orbital Angular Momentum, OAM, Magneto-Optical Kerr Effect, Magnetic Scattering, Permalloy, Artificial Spin-Ice

Patrick Montgomery
Author

11/29/2018
Date

MAGNETO-OPTICAL PROPERTIES
OF THIN PERMALLOY FILMS:
A STUDY OF THE MAGNETO-OPTICAL GENERATION
OF LIGHT CARRYING ANGULAR MOMENTUM

By

Patrick D. Montgomery

Dr. J. Todd Hastings
Director of Thesis

Dr. Aaron Cramer
Director of Graduate Studies

11/29/2018
Date

Acknowledgements

I would like to thank my advisor, Dr. J. Todd Hastings, for his time and patience as a mentor, spending time working with me in the lab, and for his invaluable advice during my research project. I would like to think Sarah Lami for spending many hours looking at my samples in the SEM with me and offering advice on my project. I would like to thank Justin Woods for creating a patterned sample for me when I did not have access to the required equipment. I would like to thank Brian Wajdyk for his advice and for providing instruction on the use of lab equipment for my project. I would also like to thank my wife, Brittany Montgomery, for her encouragement, patience, and for believing in me.

Table of Contents

LIST OF TABLES

LIST OF FIGURES

Chapter 1: Introduction

The study of magneto-optics began in the late 1800's, when John Kerr discovered the magneto-optical Kerr effect (MOKE) and Woldemar Voight discovered the Voigt effect. [1] The MOKE was studied in permalloy (Py) throughout the 20th century after its invention by Gustav Elmen between 1913 and 1916. [2] Modern research is investigating the magneto-optical generation of light carrying orbital angular momentum (OAM). Researchers are currently using x-rays to study OAM. This work hypothesizes that x-ray wavelengths of light are not required, and that the possibility exists to study this phenomenon using visible wavelengths of light (370 to 1000 nm).

1.1 Current Research

Current research is being performed by X. M. Chen et al. in order to study the effects of square lattice antiferromagnetic (AF) artificial spin-ice (ASI) structures on light with a wavelength of 500 eV (~2.48 nm). [3] The 500 eV light used in the experiments carried out by Chen is generated using a synchrotron. The square lattice structures are created using magneto-optical materials such as Py. The segments of the square lattice (see figure 1.1) make up the artificial spin-ice of the structure. In the AF ground state, the AF lattice is twice the structural lattice of the pattern. [3] The difference in the AF lattice period is responsible for magnetic scattering of 500 eV light incident on the samples. [4]

When the square lattice structure is magnetized in plane the ASI structure changes in response to magnetization. [4] Figure 1.2 shows a 3 nm thick Py lattice magnetized in plane and imaged using photoemission electron microscopy. [3] The effects of

magnetization on the sample can be seen in figure 1.2 with respect to the bright and dark segments of the pattern.

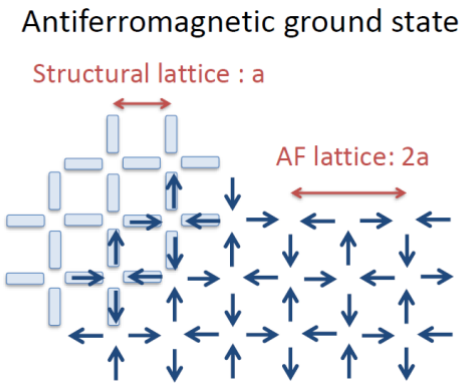

Figure 1.1: This figure shows a cartoon of a square artificial spin-ice structure in the antiferromagnetic ground state. [3] The antiferromagnetic lattice spacing is twice that of the structural lattice spacing. Figure courtesy of J. T. Hastings, X. M. Chen, et al. [3]

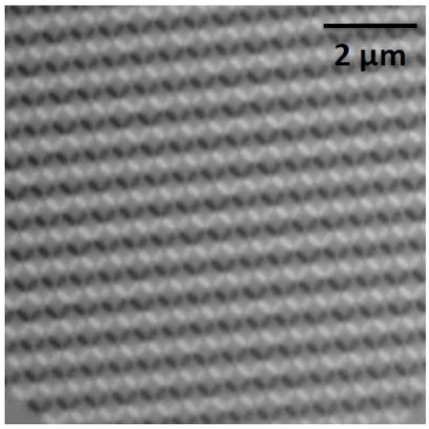

Figure 1.2: This figure shows a square artificial spin-ice structure magnetized in plane imaged using photoemission electron microscopy. [3] The dark and bright artificial spin-ice segments show the magnetization of the structure. Figure courtesy of J. T. Hastings, X. M. Chen, et al. [3]

Forked diffraction gratings are known to impart OAM on light in the x-ray spectrum (100 eV to 100 keV). [4] X. M. Chen et al. have combined forked diffraction gratings with square lattice antiferromagnetic artificial spin-ice structures in order to created two-dimensional diffraction gratings such as the one shown in figure 1.3. The study of these patterns using x-rays has yielded results consistent with both OAM and magnetic scattering due to the magneto-optical properties of Py. [3, 4] Magnetizing the two-dimensional forked diffraction patterns changes the AF state of the ASI, resulting in the manipulation of any OAM present in the half-order Bragg peak. [4] Positive OAM results from the pattern in figure 1.3 can be seen in figure 1.4.

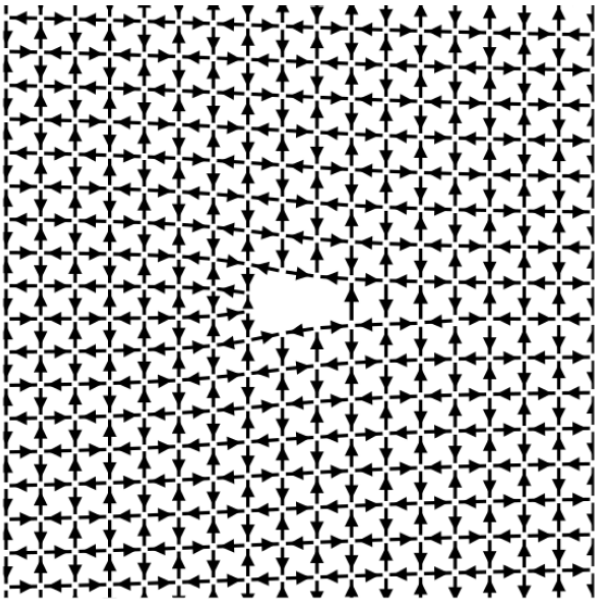

Figure 1.3: This figure shows a "square lattice with a 4π *radial phase shift in the antiferromagnetic ground state," X. M. Chen et al. [3] The same pattern was used in the experiments carried out in this work. Figure courtesy of J. T. Hastings, X. M. Chen, et al. [3]*

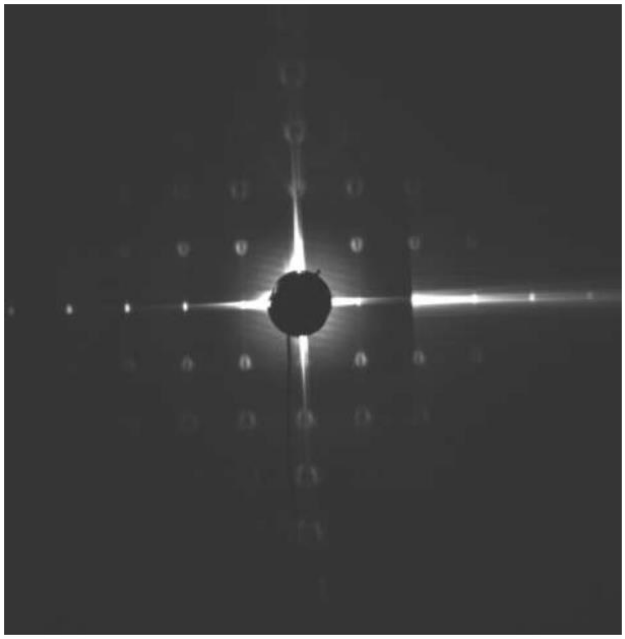

Figure 1.4: This figure shows the structural Bragg peaks at 500 eV (~2.48 nm). [3] The pattern was taken off of the Fe L-edge resonance. [4] The bright rings with a center null show evidence of OAM using x-ray wavelengths. Figure courtesy of J. T. Hastings, X. M. Chen, et al. [3]

1.2 Brief Conceptualization of Thesis

This work aims to shift some of the study of the magneto-optical generation of light carrying OAM from the x-ray spectrum to the visible spectrum of light. By using visible light, it may be possible to study this phenomenon in a standard lab rather than in a specialized lab using a synchrotron to provide an x-ray beam. This shift will provide multiple benefits to the researcher including reduced cost, more time in the laboratory with the sample, improving the ease of finding OAM diffraction patterns with the naked eye, and direct access to the sample while imaging.

A vortex beam is created when imparting OAM to light. A vortex beam rotates about the axis of propagation as shown in figure 1.5. [5, 6] The rotation of light about its axis of propagation causes destructive interference in the center of the beam. [6] The optical vortex is caused by the null created in the center of the beam. [6] A vortex beam takes the form of a bright ring of light with a center null when projected onto a flat surface. [4, 5, 6]

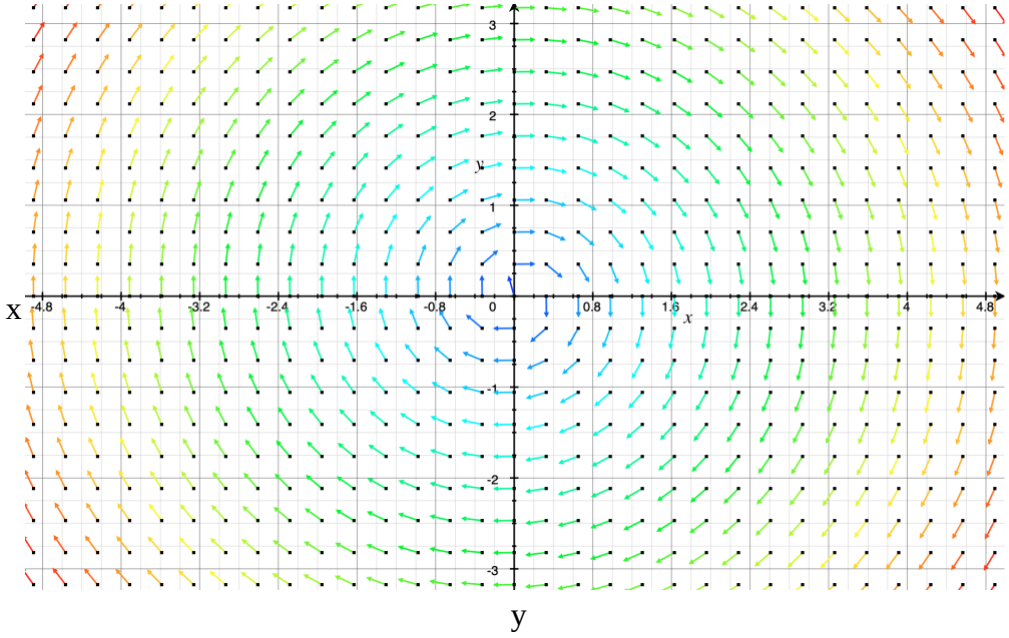

Figure 1.5: An example of the vector field of a vortex beam rotating about the axis of propagation when viewed parallel to the axis of propagation. In this figure the axis of propagation is perpendicular to the xy plane at the origin. The arrows represent the direction of the vector field at each point. The color represents the intensity of the light generated by the beam. The blue arrows represent where the null will be present due to destructive interference. The orange and yellow arrows represent where the bright ring will be due to constructive interference.

It is known from previous work by X. M. Chen et al. that two-dimensional forked diffraction gratings generate intensity patterns consistent with OAM in the 500 -700 eV range. [3, 4] This work aims to determine the validity of creating a vortex beam in the visible spectrum of light using a two-dimensional square lattice with a 4π radial phase shift in the antiferromagnetic ground state such as the one shown in figure 1.3. [3] Imaging a pattern caused by a vortex beam diffracted from this structure will show that it is possible to create intensity patterns consistent with OAM in the visible spectrum of light.

Magnetic scattering is present in diffraction from magneto-optical materials such as Py. It is hypothesized that due to magnetic scattering, a magnetic half-order Bragg peak should be present when visible light is incident on a sample such as that shown in figure 1.3. It is also hypothesized that the manipulation of the half-order Bragg peak should be possible in visible light when the ASI structure is magnetized. If the half-order Bragg peak is observed, then magnetizing the structure is expected to result in the absence of the half-order diffraction pattern.

Additional hypotheses investigated in this work include the expected presence of the OAM ring pattern in the half-order peak, and the change in the half-order peak with time due to thermal fluctuations and demagnetization. These can only be investigated if the previous hypotheses are proved valid.

1.3 Chapter Overview

This work contains five chapters. The first chapter is the current chapter, the introduction. The introduction briefly describes current research leading up to this work,

orbital angular momentum, and other relevant background information. The introduction also includes the conceptualization of this thesis and the hypotheses investigated by this work.

Chapter 2 describes the experimental methods used to conduct the research described in this work. These methods include sputtering, XRR, ellipsometry, spin-coating, electron beam lithography, and an optical bench setup. Each method is described in sufficient detail to inform the unfamiliar reader with enough information to understand the methods used at a basic level.

Chapter 3 provides a detailed description of the experimental procedures used. Each experiment, material, and all equipment used are provided in Chapter 3. This chapter is written so that each experiment should be repeatable from the information provided. The experimental parameters investigated are listed in the end of Chapter 3 in section 3.3.

Chapter 4 includes the results, analysis, and discussions pertaining to the data acquired using the procedures outlined in Chapter 3. The results attained from the parameters investigated in section 3.3 are each described in detail in Chapter 4. The results from Chapter 4 will be used to draw conclusions based on this work in Chapter 5.

Chapter 2: Experimental Methods

2.1 Introduction

This chapter discusses the methods used in each of the experiments performed. A brief description of each method will be discussed. The equipment used in each experimental method is also outlined in the following sections.

2.2 Sputtering Overview

Sputtering was performed with an AJA International ACT 1800 sputtering machine located in the Center for Advanced Materials (CAM) at the University of Kentucky, and a Hummer Turbo Sputtering System located in the Center for Nanoscale Science and Engineering (CeNSE) at the University of Kentucky. An ionization sputtering method was used to deposit thin Py films with an Al capping layer onto Si substrates. These sputtering machines use a vacuum chamber with Ar plasma at room temperature.

Sputtering is made possible by igniting a gas such as Ar to create plasma inside of a vacuum chamber. Ions from the plasma are accelerated into a target material such as Py or Al. Accelerated ions erode the target material, causing particles of the material to detach and travel through the vacuum until contacting a barrier. A thin film can be formed by placing a substrate such as Si in the path of the ejected particles of the target material. In order to deposit a thin film of uniform thickness, the substrate can be rotated in the vacuum chamber during the sputtering process. [7]

In order to minimize the time between the deposition of Py and Al, confocal sputtering was used for non-patterned samples. Confocal sputtering uses multiple sputtering sources aimed at a common focal point in order to deposit multiple layers while minimizing contaminants. [7] A direct sputtering method was used for patterned samples. Direct sputtering uses one sputtering source aimed directly at the substrate.

Figure 2.1 shows a cross section example by layer of the sputtered samples used in this work. The layers include a Si substrate with a SiO_2 oxidation layer, a Py (NiFe) thin film, and Al_2O_3 capping layer.

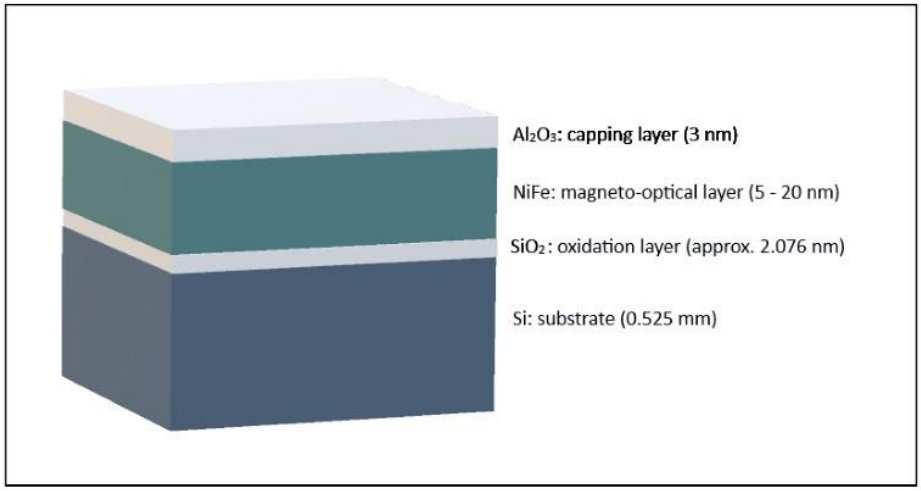

Figure 2.1: Cross section example of samples with Py (NiFe) and Al_2O_3 deposition. Figure not to scale.

2.3 XRR Overview

A Brunker D8 Advance Plus was used for the x-ray reflectometry (XRR) measurements in this experiment. X-ray reflectometry works by placing a sample on a stage, emitting x-rays through a slit at an angle incident to the sample, and then detecting

the intensity of the reflected x-rays. [8] Material thickness can be determined by measuring the intensity of the reflected x-rays in a range of angles and plotting the relationship on a semi-log plot. [8]

The thickness of a sample is calculated using Bragg's Law (eqn. 2.1). The semi-log plot results in a graph with multiple peaks and troughs. The change in the angle between two peaks can be represented as the angle θ. In the software used for this experiment, the x-axis was represented as 2θ, which had to be divided by 2 before using it in Bragg's Law.

Bragg's Law was solved for thickness as shown in equation 2.2, where d is the thickness of the Py layer, λ is the wavelength, n is refractive index, and θ is the angle determined graphically.

$$2dsin\theta = n\lambda \qquad \textit{eqn. 2.1}$$

$$d = \frac{n\lambda}{2sin\theta} \qquad \textit{eqn. 2.2}$$

The graphical data was fit to a model of each sample in Leptos 7 modeling software to show an estimated Py thickness. The models used a Si substrate model with a SiO_2 oxidation layer, and a Py layer. The true Py thickness was calculated using the average value of equation 2.2 for each peak-to-peak region of the graph using experimental data.

2.4 Ellipsometry Overview

Ellipsometry data was gathered using J.A. Woollam M-2000 and Gaertner L117 ellipsometers located in the Center for Nanoscale Science and Engineering (CeNSE) at the University of Kentucky, and a VASE ellipsometer located in the Micro Nano Technology Center at the University of Louisville. Spectroscopic ellipsometry was used to acquire data on each sample. Variations of isotropic, anisotropic, and Mueller matrix scan types were used to acquire specific data.

An ellipsometer measures the changes in polarization of the light reflected off of a substrate or sample. [9] The polarization state is measured by the Ψ and Δ parameters, where Ψ represents an amplitude ratio, and Δ represents the phase difference between s and p polarized light. [9, 10, 11] The Ψ and Δ data obtained by the ellipsometer can be used to calculate the optical properties (n and k), estimate thickness, and to determine other material properties of a sample. [10]

Figure 2.2 shows an example of linearly polarized light reflected off of a sample. [12] The reflected light undergoes both an amplitude and phase change. [12] As seen in the figure, s and p polarized light can be represented by the s and p planes. When the s and p phases change, the direction of polarization is changed. The ellipsometer measures the phase difference between the reflected s and p polarized light as Δ.

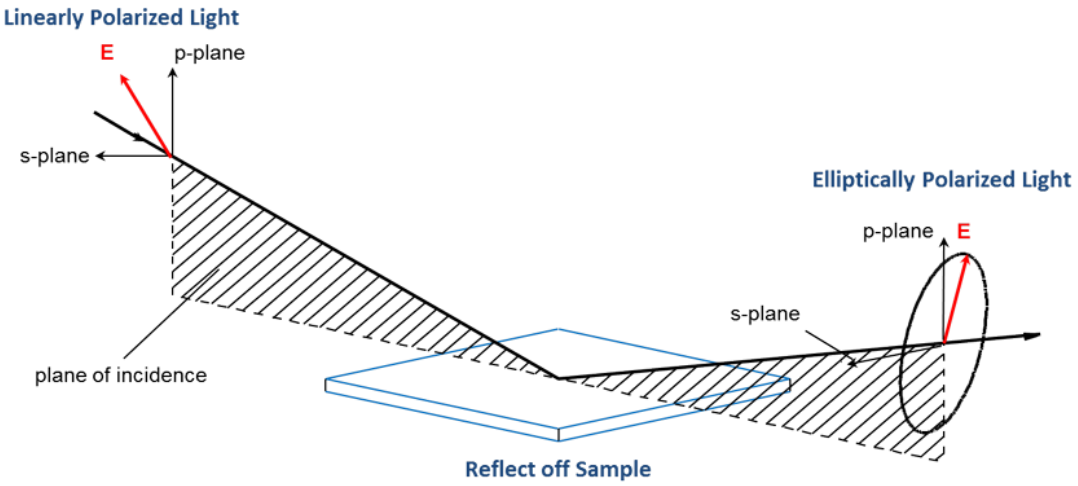

Figure 2.2: This figure shows the s and p planes of polarized light. Figure courtesy of J.A. Woollam Co. [12]

2.5 Spin-coating Overview

In order to perform electron beam lithography on a sample, the sample must first go through a process called "spin-coating". Spin-coating includes placing a clean substrate into a device called a spin coater. The spin-coater holds the sample in place via a vacuum pump. A resist such as PMMA is coated onto the substrate. The spin-coater then spins the substrate at a high velocity. The thickness of the desired resist depends on the RPM of the spin-coater. The process of spin-coating results in a resist of desired thickness on the substrate.

2.6 Electron Beam Lithography Overview

Electron beam lithography (EBL) was performed using a Raith EBL in the Center for Nanoscale Science and Engineering (CeNSE) at the University of Kentucky.

Additional patterned samples were provided from Argonne National Laboratory when the Raith EBL at CeNSE was undergoing maintenance.

Electron beam lithography works by inserting a substrate coated with a resist material such as PMMA into a vacuum chamber. A pattern is uploaded into the EBL software. Dose, dwell time, and beam current are set with respect to the desired results. The EBL then "prints" the pattern by using a highly focused electron beam to bombard the resist material with electrons. [13] The electron exposure modifies the solubility of the resist material. [13]

Once the sample has been "printed" by the EBL, it is inserted into a developing solution. The developing solution dissolves the exposed resist, leaving the desired pattern in the resist material. The sample can then undergo a metal deposition in a process such as sputtering. The deposited material will adhere to the resist, and the substrate. The sample is then placed in a solution to dissolve the remaining resist material in a process called "lift-off." After lift-off, the remaining metal deposition will be in the form of the desired pattern. Figures 2.3 and 2.4 show a cartoon of this process, as well as a developed sample from this experiment.

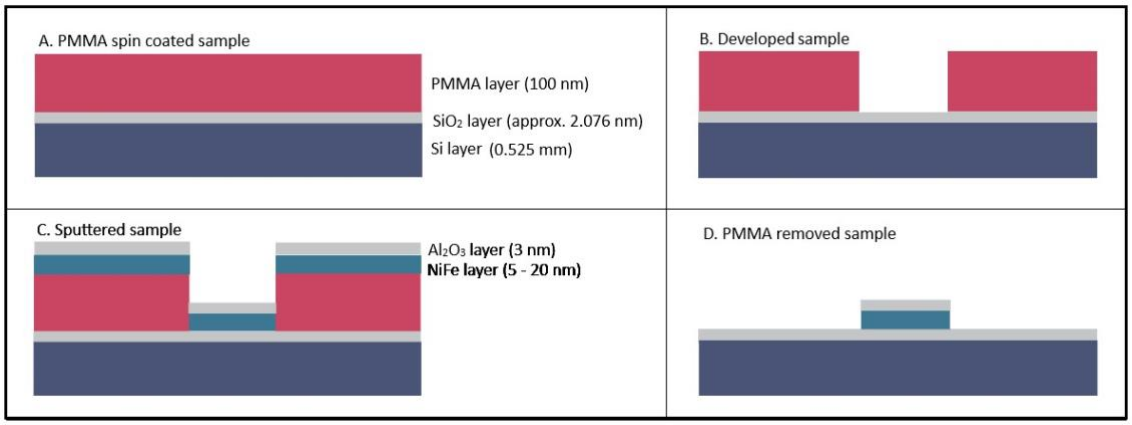

Figure 2.3: This figure shows a cross section of a sample undergoing the EBL procedure. A) First the substrate undergoes spin-coating to obtain a 100nm PMMA layer. B) The sample is then placed into the EBL, where the desired pattern is printed onto the sample. Once removed from the EBL, the pattern is developed and the PMMA in the developed area is removed. C) The sample undergoes Py (NiFe) and Al deposition through a process such as sputtering. The Al will oxidize and form Al_2O_3. D) The remaining PMMA is removed. The Py and Al depositions remain in the developed area. The result is a deposition that is in the form of the desired pattern. Figures are not to scale.

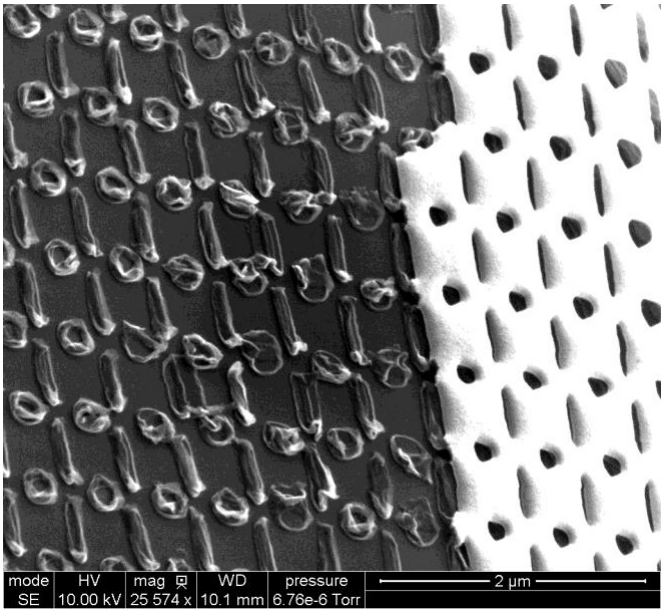

Figure 2.4: This figure shows a sample after the EBL and development procedures. The right side of the figure shows the PMMA resist with the developed pattern. The left side of the figure shows the substrate with Py and Al deposition post lift-off.

2.7 Using an Optical Bench Set-up to Detect OAM and Half-order Diffraction

A Thorlabs TLS001-635 635 nm laser and a Point Grey GS3 camera were set up on an optical bench. The camera was connected to Spinnaker SDK software to capture the diffracted image. The laser was focused onto a patterned sample using a 200mm focal length lens. The diffracted light was captured by the camera in order to look for orbital angular momentum (OAM). The bench set-up is shown in figure 2.5.

In order to detect the half-order Bragg peak, the estimated angle was calculated by solving the grating equation (eqn. 2.3) for the angle of diffraction (eqn. 2.4). The camera was rotated to the estimated angle and adjusted accordingly to look for the diffracted light pattern.

$$n\lambda = d(sin\theta_i + sin\theta_d) \qquad \textit{eqn. 2.3}$$

$$\theta_d = sin^{-1}\left(\frac{n\lambda}{d} - sin\theta_i\right) \qquad \textit{eqn. 2.4}$$

In equations 2.3 and 2.4 n is the diffraction order, λ is the wavelength, d is the distance between elements in the pattern, θ_i is the angle of incidence, and θ_d is the angle of diffraction.

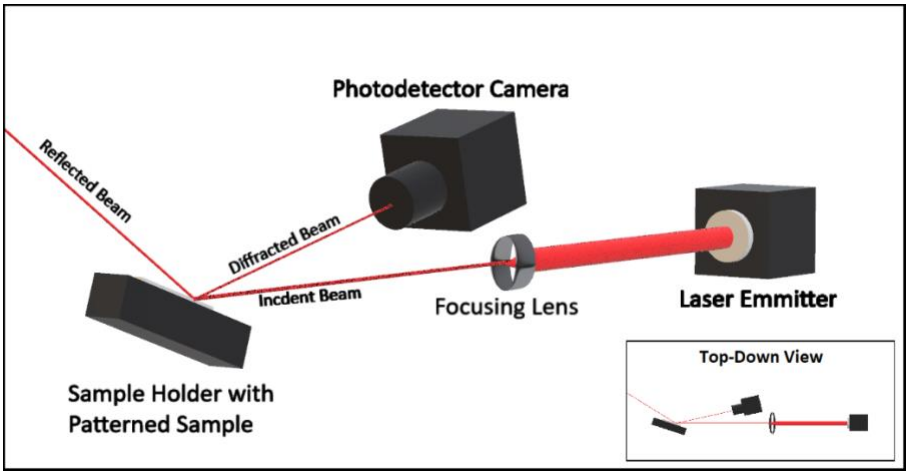

Figure 2.5: This figure shows the optical bench set up consisting of the laser, focusing lens, sample, and camera. Figure not to scale.

Chapter 3: Experimental Procedure

3.1 Introduction

The procedures used in each part of this research are outlined in this chapter. Substrate and Py material models were created for use in experiments. The thickness and optical parameters of samples were determined by fitting material models to experimental data. These models were also used to compare the magneto-optical effects of Py on visible light.

After establishing the optical properties of the materials used in this research, the effects of magnetization on the magneto-optical properties of Py on visible light were investigated. Thin Py films were magnetized and the phase differences of polarized visible light reflected off of samples pre and post magnetization were measured. The Voigt parameter (Q) and the permittivity matrix for Py were investigated using experimental data.

Py OAM patterns were created on Si substrates using electron beam lithography. A laser was pointed at the Py patterns in order to produce diffraction patterns. The diffraction patterns were imaged using a photodetector camera. Diffraction patterns indicating orbital angular momentum were studied. The half order diffraction patterns were investigated.

3.2 General Procedure

First, an experimentally based substrate model was created in order to maintain consistent, accurate, and reliable sample models for use in both ellipsometry and x-ray

reflectometry experiments. A 0.525 mm Si (100) wafer was used as a base substrate. Si oxidizes and forms a SiO_2 layer when exposed to oxygen. Si and SiO_2 must be accounted for in order to create an accurate substrate model.

The substrate was divided into multiple 1 cm^2 samples. Three of the divided samples were randomly selected. The thickness of the SiO_2 layer was measured using a J.A. Woollam M-2000 ellipsometer located in the Center for Nanoscale Science and Engineering (CeNSE) at the University of Kentucky.

A spectroscopic scan was performed on each of the three random samples. These samples are referred to as samples 1, 2 and 3. The SiO_2 measurements of each sample can be found in table 3.1. The average SiO_2 thickness of these samples was calculated as 2.076 nm with a variance of 0.015 nm. The error was given by the VASE software.

Table 3.1: Thickness measurements of SiO_2 used to create a substrate model. Note: The values reported in tables are rounded to three significant figures. Therefore, some numbers in tables may appear slightly different that the numbers used to create experimental models.

	Estimated Si thickness (mm)	**Measured SiO_2 thickness (nm)**	**Error (nm)**
Sample 1	0.525	2.22	0.00255
Sample 2	0.525	2.01	0.00243
Sample 3	0.525	2.00	0.00249
Average	0.525	2.08	0.00249
Variance	0	0.015	3.6E-9

The substrate model was created using VASE modeling software which contained layer models for both Si and SiO_2. The thickness of the Si model layer was fixed to 0.525

mm. Due to light absorption in Si, a 0.525 mm wafer can be considered semi-infinite with regard to its optical parameters. In the VASE modeling software there is no change in the Si layer model with a thickness greater than 10^{-3} nm. Because the Si substrate exceeded 10^{-3} nm, using 0.525 mm was sufficient for use in the Si layer model without measuring the exact thickness.

A fixed 2.076 nm SiO_2 layer was overlaid on a fixed 0.525 mm Si layer. The composite substrate model was saved for future use. While the exact SiO_2 thickness may vary for each sample, the model is reasonable because the 0.015 nm variance does not create a significant change in the optical properties of the model.

Next, three Si substrates were sputtered with Py in an AJA International ACT 1800 sputtering machine. These samples are referred to as samples 4, 5, and 6. The sputtering conditions for each sample were identical and are listed in table 3.2.

Table 3.2: Sputtering conditions of samples 4, 5, and 6.

	Height (mm)	**Rotation**	**Time (s)**	**Pressure (mTorr)**	**Power (W)**
Strike	5	On	120	5	30
Pre-sputter	5	On	120	3	30
Deposition	5	On	900	3	30

The VASE modeling software used with the J.A. Woollam M-2000 ellipsometer did not contain a Py model that sufficiently matched the optical characteristics of the Py used. In order to create a new material model in VASE, the thickness of the sample material must be known. The deposition rate of Py in the sputtering machine was not known, so an alternate method was needed to determine the thickness of the Py samples.

X-ray reflectometry was used to measure the thickness of the samples 4, 5, and 6. The first sample was placed onto the stage of the x-ray reflectometer. A 0.1 mm Cu filter was inserted in front of the x-ray emitter. The stage was positioned so that half of the x-rays from the emitter collided with the sample at $\theta = 0°$, where $0°$ is in the sample plane. After reflecting from the sample, the x-rays passed through a 0.1 mm slit before entering a detector. The intensity was measured between $0°$ and $2.5°$ with respect to the sample plane.

The intensity was plotted with respect to 2θ, where 2θ is twice the angle at which the intensity was measured. Figure 3.1 shows the semi-log plot of x-ray intensity vs. 2θ along with various parameters of the XRR scan of sample 6. The thicknesses of the samples were calculated using Bragg's Law (eqn. 2.2) as discussed in Section 2.3 of Chapter 2. The Py deposition rate was then calculated in order to accurately deposit known film thicknesses in future experiments.

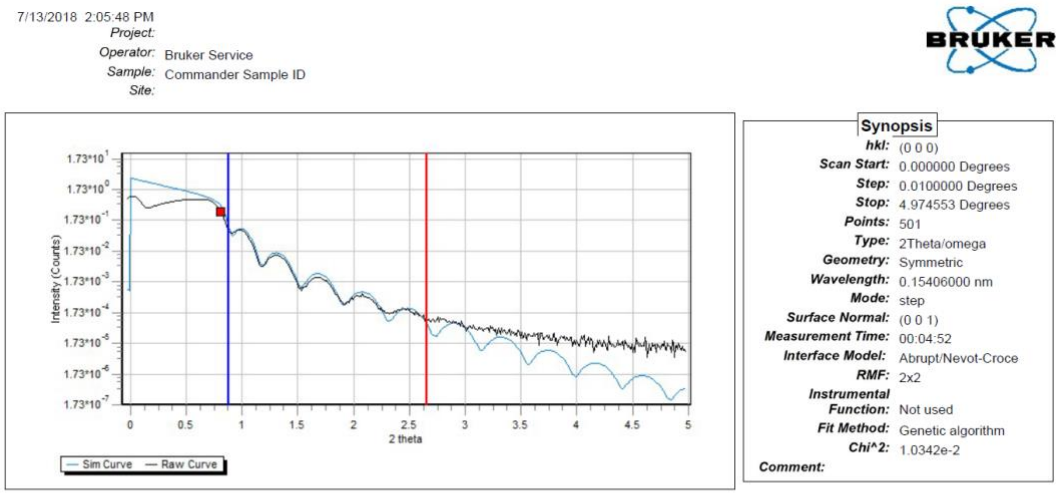

Sample

N	R	Material	Cell input	Thickness	Roughness	Conc X Top, %	Conc X Bot, %	Relax. Top	Relax. Bot	Profile	Grading	Density T
1	1	Py	density	20.3677	0.0000	0.0000	0.0000	0.000	0.000	No Gradient	10	8.74000
2	1	SiO2	density	2.0760	0.0000	0.0000	0.0000	0.000	0.000	No Gradient	10	2.65000
SUB	1	Si	density	0.0000	0.0000	0.0000	0.0000	0.000	0.000	No Gradient	0	2.32910

Figure 3.1: Sample 6 thickness measurements and semi-log plot using XRR.

After measuring the Py sample thicknesses, it was possible to create a Py material model in the VASE software. Sample 4 was spectroscopically scanned by the M-2000 ellipsometer from 45 to 85 degrees to gather Ψ and Δ experimental data. The experimentally created substrate model was used for the sample 4 substrate model. A Py dummy layer was placed on top of the substrate model. The thickness of the Py dummy layer was fixed based on the measured thickness from the x-ray reflectometry experiment. The Lorentz Oscillator parameters of the Py dummy layer were allowed to vary and were fit to the experimental data. The optical properties, n and k, were then calculated from the Lorentz Oscillator parameters within VASE. This procedure was repeated for samples 5 and 6. The average n and k values of samples 4, 5, and 6 were used to create an optical model for Py in VASE.

Four new substrates were sputtered with Al in the AJA International ACT 1800 sputtering machine. These samples are referred to as samples 7, 8, 9, and 10. The sputtering conditions for each sample were identical with the exception of time and are listed in table 3.3.

Table 3.3: Sputtering conditions of samples 7, 8, 9, and 10.

	Height (mm)	**Rotation**	**Time (s)**	**Pressure (mTorr)**	**Power (W)**
Strike	5	On	120	5	30
Pre-sputter	5	On	120	0.5	30
Deposition	5	On	Varies	0.5	30

The thickness of the sputtered Al and Al_2O_3 in each sample was measured using the M-2000 ellipsometer and the VASE modeling software. Sample 7 was placed on the stage of the ellipsometer. A spectroscopic scan from 45 to 85 degrees was performed. The VASE modeling software contained layer models for both Al and Al_2O_3. The Al_2O_3 layer is necessary due to the rapid oxidation of the thin Al layer. The Al_2O_3 model layer was overlaid on the Al model layer. The resulting composite layer was overlaid on the experimentally based substrate model.

Estimates of the Al and Al_2O_3 thicknesses were entered into the VASE model. The thicknesses of the Si and SiO_2 substrate were fixed, and the Al and Al_2O_3 thicknesses were allowed to vary. A normal fit was performed in order to fit the optical properties of the model to the experimental data. The resulting fit showed the estimated thickness measurements of Al and Al_2O_3 for sample 7. This procedure was repeated for samples 8,

9, and 10. The Al deposition rate was then calculated in order to accurately deposit known film thicknesses in future experiments.

Based on the calculated deposition rates of Py and Al, Py films of approximately 20, 10, and 5 nm with a 3 nm Al capping layer were deposited onto three new substrates. These samples are referred to as samples 11, 12, and 13 respectively, and the deposition conditions of these samples and thickness measurements can be found in table 3.4.

Table 3.4: Sputtering deposition conditions and thickness measurements of samples 11, 12, and 13. Note: The Al deposition thickness measured in the table consisted of entirely Al_2O_3 due to the complete oxidation of the Al layer.

	Height (mm)	**Rotation**	**Time (s)**	**Pressure (mTorr)**	**Power (W)**	**Estimated Thickness (nm)**	**Measured Thickness (nm)**
Sample 11							
Py Strike	5	On	120	5	30	-	-
Py Pre-sputter	5	On	120	3	30	-	-
Py Deposition	5	On	880	3	30	20.0	20.8
Al Strike	5	On	120	5	30	-	-
Al Pre-sputter	5	On	120	0.5	30	-	-
Al Deposition	5	On	125	0.5	30	3.00	1.42
Sample 12							
I	5	On	120	5	30	-	-
Py Pre-sputter	5	On	120	3	30	-	-
Py Deposition	5	On	440	3	30	10.0	11.5
Al Strike	5	On	120	5	30	-	-
Al Pre-sputter	5	On	120	0.5	30	-	-
Al Deposition	5	On	125	0.5	30	3.00	1.56
Sample 13							
Py Strike	5	On	120	5	30	-	-
Py Pre-sputter	5	On	120	3	30	-	-
Py Deposition	5	On	220	3	30	4.99	6.59
Al Strike	5	On	120	5	30	-	-
Al Pre-sputter	5	On	120	0.5	30	-	-
Al Deposition	5	On	125	0.5	30	3.00	1.58

In order to verify the calculated deposition rates and the Py material model in VASE, the thicknesses of samples 11, 12, and 13 were measured using the M-2000 ellipsometer. Sample 11 was measured using a spectroscopic scan to gather experimental data. A model was constructed in VASE using the experimentally created substrate model, a Py layer, an Al layer, and an Al_2O_3 layer. The thickness estimates of each layer (listed in table 3.4) were entered into the model, with an estimated Al layer of 0 nm and Al_2O_3 layer of 3 nm for each model. The Al layer was estimated to be 0 nm because full oxidation of the thin Al layer was expected. The substrate thickness was fixed and the Py, Al, and Al_2O_3 thicknesses were allowed to vary. A normal fit was performed, fitting the optical properties of the model to the experimental data. This procedure was repeated for samples 12 and 13. The thickness measurements for each layer were reasonable based on the calculated deposition times. The Py layers were within 2 nm of estimated values, which is sufficient for the parameters studied.

The next step was to study the magneto-optical effects of Py. This was done by magnetizing samples 4, 5, 6, 11, 12, and 13 using a Danfysik 854T electromagnet in the Chemistry Physics building at the University of Kentucky. The samples were placed in an orientation so that the north and south poles were known. The samples were magnetized in plane using a magnetic field of 0.29 ± 0.02 T. The samples were left in the field for 5 minutes each in order for them to become magnetically saturated.

Samples 4, 5, 6, 11, 12, and 13 were scanned in a north-south orientation, then in a south-north orientation using an anisotropic spectroscopic scan with the M-2000 ellipsometer in order to study the Δ parameter. The samples showed interesting data characteristics in the Δ parameter immediately after magnetization, but upon performing

subsequent scans these data characteristics were not repeatable. According to Colonel Wm. T. McLymen, 78-Py has a saturation of 0.75 T. [2] The Py used was 80-Py, which should have a similar saturation point.

To account for the higher than expected saturation point, the samples were placed in a magnetic field of 0.80 ± 0.01 T to become magnetically saturated. In order to sustain magnetization in an 80-Py sample, saturation at 0.75 T must be achieved.

After re-magnetizing samples 4, 5, 6, 11, 12, and 13 the Δ parameter was examined in the previous way by rescanning the samples using the M-2000 ellipsometer. The change in polarization due to magnetization was studied by using a Gaertner L117 ellipsometer located in CeNSE at the University of Kentucky. The ellipsometer was used to look for polarization extinction and maximums in order to determine Ψ and Δ, which are calculated using equations 3.1 and 3.2. In equations 3.1 and 3.2 A_1 and A_2 are the analyzer angles at extinction, and P_1 and P_2 are the polarizer angles at extinction.

$$\Psi = \frac{180° - (A_2 - A_1)}{2} \qquad \textit{eqn. 3.1}$$

$$\Delta = 360° - (P_1 + P_2) \qquad \textit{eqn. 3.2}$$

The Gaertner L117 ellipsometer used a 632.8 nm HeNe laser incident to the sample at 70°. The laser passed through a polarizer before reflecting off of the sample. The reflected light passed through an analyzer before the intensity of the beam was displayed on a scale with no units. The polarizer and analyzer were manually adjusted to

find the lowest possible intensity, called extinction. The angle of the polarizer and analyzer at extinction were recorded as A_1 and P_1.

After recording A_1 and P_1, the polarizer was rotated to $P_1 + 90°$, and the analyzer was rotated to $180° - A_1$. The polarizer and analyzer were once again adjusted in order to find extinction. The angle of the polarizer and analyzer were recorded as A_2 and P_2. The maximum values were found by setting the polarizer and analyzer to 45°, and manually adjusting the analyzer to find the maximum intensity.

After studying the magneto-optical effects of non-patterned samples, patterned samples were created using electron beam lithography (EBL). The first step in creating a patterned sample is to clean the substrate, and spin-coat a resist material onto the sample.

A high resolution polymethyl methacrylate (PMMA) resist was used for the patterned samples. Si substrates were cleaned using acetone, IPA, and distilled water before being dried with nitrogen and being placed on a hotplate. Once dry, the substrates were placed into a spin-coater (one at a time) and centered so that the process would create an even resist layer. PMMA resist was placed over the entirety of each substrate in order to provide the most even coating possible. The substrates were spun at 4000 rpm in order to create a resist thickness of approximately 100 nm. The substrates were then placed on a hotplate with a temperature of 322 K for a one-minute post bake.

A Raith EBL was used to create patterned samples in this experiment. The pattern printed using EBL can be seen in figure 3.2. A Si substrate with PMMA resist was loaded into the EBL vacuum chamber. The beam characteristics were adjusted, which included modifying the beam dose, beam current, dwell time, stigmation, and accelerating voltage.

A detailed breakdown of the beam characteristics and adjustments is outlined in section 3.3.5.

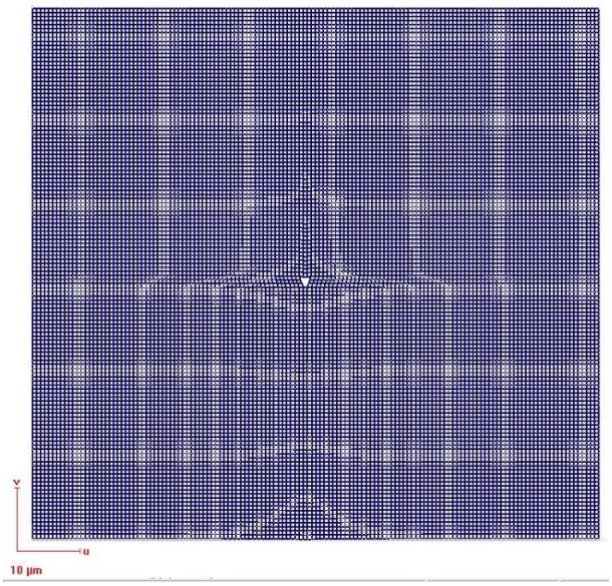

Figure 3.2: The diffraction pattern printed onto the samples using EBL. Note: The elements of this pattern are nanoscale and are not clearly represented in full detail in the figure.

In order to determine the optimal beam current and dwell times, 11 patterns with different beam doses and accelerating voltages were printed onto multiple substrates. The optimal electron beam parameters were determined by examining each pattern after development. All samples were developed using a MIBK/IPA 1:3 chemical bath for 1 minute.

After determining the optimal electron beam parameters and accelerating voltage, a new sample, referred to as sample 17, was printed with two copies of the pattern. Sample 17 was developed before being sputtered with Py and Al using a Hummer Turbo

Sputtering System. The deposition conditions of the patterned sample 17 are shown in table 3.5. The Hummer Turbo Sputtering System was used on the patterned samples because it uses a direct sputtering method. Direct sputtering is a sputtering method where the target is pointed directly at the sample. Confocal sputtering was used in the non-patterned samples to reduce contaminants. Confocal sputtering points the target at an angle to the sample and can produce undesirable results in patterned samples as shown in figures 3.3 and 3.4. Py and Al can build up on the "walls" of the PMMA because confocal sputtering deposition takes place at an angle.

In order to determine the Py and Al thickness of patterned sample 17, an additional Si substrate was sputtered at the time of deposition. The deposition thickness of sample 17 was determined by measuring the thickness of the additional substrate using the M-2000 ellipsometer. The thickness measurements can be found in table 3.5.

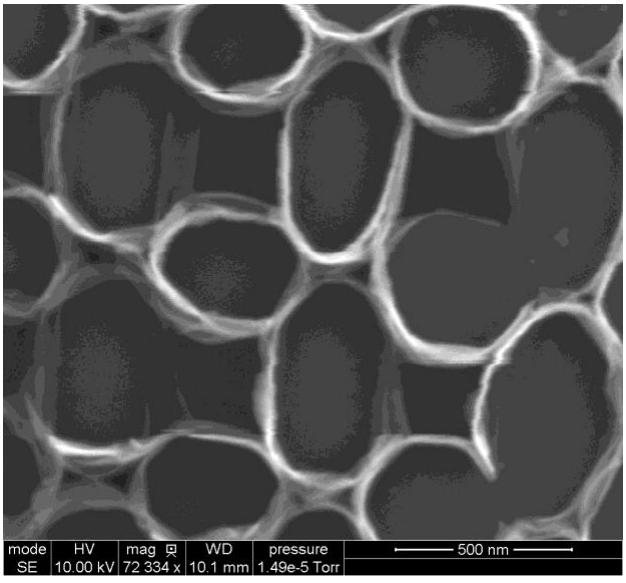

Figure 3.3: This figure shows a sample where the metals adhered to the sides of the PMMA during sputtering deposition, resulting in an undesirable outcome.

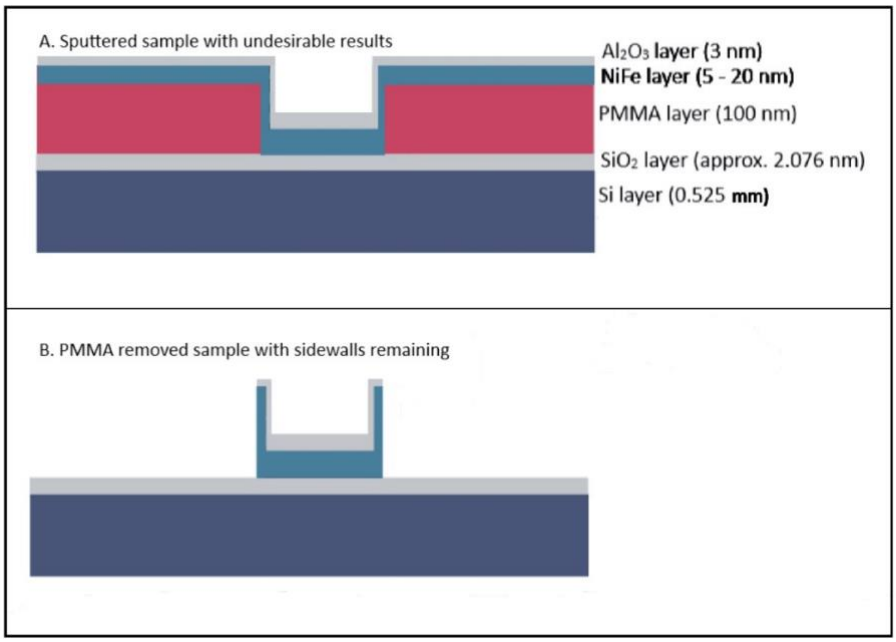

Figure 3.4: Cross section of a sample from EBL procedure. A) When sputtering the developed sample, Py and Al_2O_3 adhered to the sides of the remaining PMMA Layer. B) When remaining PMMA is removed, sidewalls remain on the sample. This is undesirable and can affect the diffraction pattern. Figures are not to scale.

Table 3.5: Deposition conditions of sample 17.

	Height (mm)	**Rotation**	**Time (s)**	**Pressure (mTorr)**	**Power (W)**	**Estimated Thickness (nm)**	**Measured Thickness (nm)**
Py Strike	5	Off	120	3.65	90	-	-
Py Pre-sputter	5	Off	120	3.65	90	-	-
Py Deposition	5	Off	1580	3.65	90	10.3	8.93
Al Strike	5	Off	120	4.49	90	-	-
Al Pre-sputter	5	Off	120	4.49	90	-	-
Al Deposition	5	Off	270	4.49	90	3	2.65

After deposition, sample 17 was soaked in an A Thinner bath until all of the PMMA achieved lift-off and only the Py and Al pattern was left on the substrate. The sample was cleaned using IPA and distilled water before being dried on a hotplate at 322 K.

A Thorlabs TLS001-635 635 nm laser was set up on an optical bench. A 200 mm focusing lens was placed 15 cm from the laser. Sample 17 was placed on a vertical mount 20 cm from the focusing lens. The optical bench setup is shown in figure 2.5, not to scale. The sample was rotated so that the incident beam would hit the sample at approximately 45°. The angle normal to the sample plane was considered as 0°. The sample was then manually adjusted until the incident beam completely covered the entire OAM pattern. The incident beam was considered to cover the entire pattern when the reflected beam produced a pattern of concentric dark and bright rings (figure 3.5).

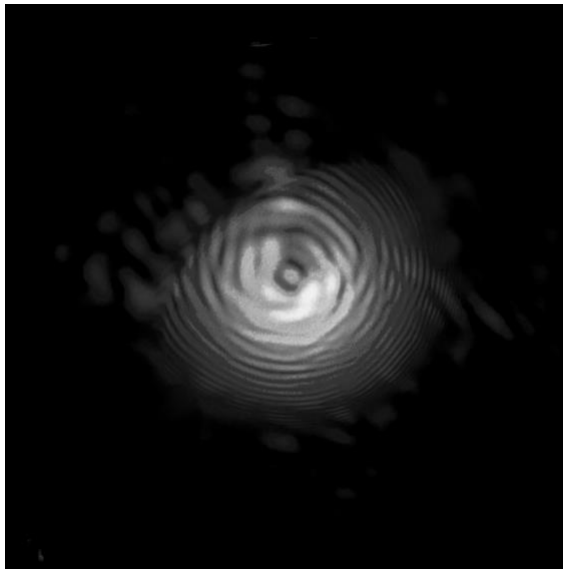

Figure 3.5: This figure shows the reflected pattern from a 635 nm laser incident to the patterned sample at 45°.

Using equation 2.4, the first-order Bragg peak was expected at 16.3° because the lattice periodicity of the diffraction pattern was measured as 642.85 ± 0.6 nm. The Point Grey GS3 camera was placed at 16.3° to capture the diffraction pattern. The Point Grey camera was placed as close to the sample as possible in order to capture the entire diffraction pattern. The exposure time of the camera was set to continuous, and the intensity of the laser was reduced to capture the highest quality image possible of the diffraction pattern.

After capturing images of the first-order Bragg peak, the half-order Bragg peak was examined. The half-order Bragg peak was expected at -12.31° using equation 2.4. The Point Grey GS3 camera was placed at -12.31° to capture the half-order diffraction pattern. The Point Grey camera was manually adjusted to produce the highest quality image capture by placing it as close to the sample as possible. The exposure time of the camera was then set to continuous to capture the highest quality image of the diffraction pattern.

The patterned samples created at the University of Kentucky contained imperfections due to errors with the z-stage controller in the EBL, as well as sputtering. After collecting data from sample 17, patterned samples could no longer be produced at the University of Kentucky because of ongoing maintenance on the Raith EBL. The pattern was sent to Argonne National Laboratory, which produced a sample (referred to as sample 18) without the imperfections due to the z-stage controller and sputtering.

According to the manufacturer of the sample at Argonne National Laboratory, the OAM diffraction patterns on sample 18 consists of 3 nm of Py, and 2 nm of Al_2O_3. The sample was created using a similar Raith EBL. The metal layers on sample 18 were

deposited using an electron beam evaporator. An electron beam evaporator heats a target metal to a high temperature inside a vacuum until target metal evaporates. The evaporated metal, such as Py, then adheres to the substrate and transitions back to a solid state. This method can provide very precise results in patterned samples.

Sample 18 contained 9 OAM patterns, and a 10^{th} annealing control pattern. A similar optical bench setup was used for sample 18, with the addition of a Proscope 3 microscope, a rotating base under the sample stage, a computer-controllable rotating camera stage, and an aperture for the laser. The sample stage with x, y, and z control was centered over the rotating camera stage. The sample stage was mounted on a rotating base with a Vernier scale so that the angle of incidence could be precisely adjusted. A microscope was set up in order to identify which of the 10 patterns were being imaged at any time. The microscope was mounted so that it could be easily rotated away from the sample. The camera was mounted on a rotating stage centered underneath the sample. The camera stage was controlled with a computer to place the camera at precise angles. An aperture was added to ensure that the beam covered the entire pattern. A re-creation of this optical bench setup can be seen in figure 3.6. The sample was placed on a rotating platform with an axis of rotation perpendicular to the sample plane when installed on the stage.

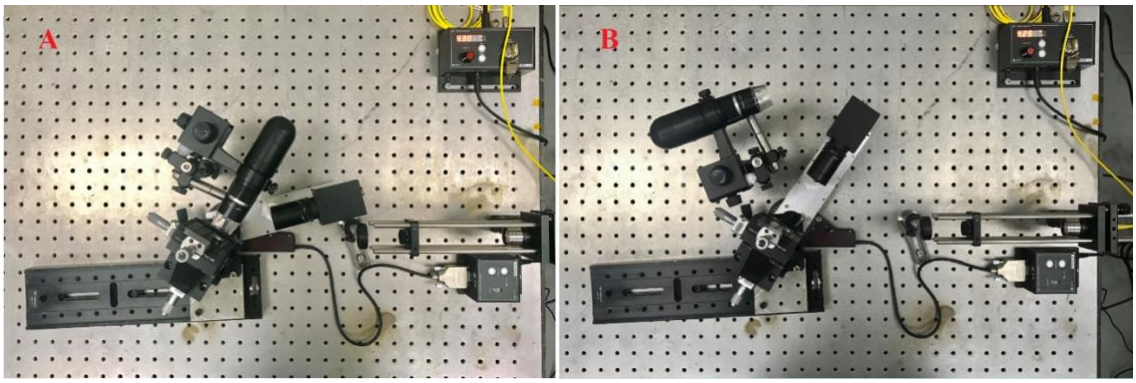

Figure 3.6: A re-creation of the optical bench setup for sample 18. A) The microscope used to view the sample and align the laser with the patterns. B) The microscope is rotated away from the sample and the camera is positioned via the stage controller.

Sample 18 was rotated so that the incident beam would hit the sample at 60°. The angle normal to the sample plane was considered as 0°. The microscope was adjusted so that all 10 OAM patterns on the sample were visible. The sample was then adjusted using the stage controllers until the incident beam completely covered the first OAM pattern. The incident beam was considered to cover the entire pattern when the diffraction pattern was symmetrical.

Using equation 2.4, the first-order Bragg peak was expected at 6.78° because the lattice periodicity of the diffraction patterns of sample 18 were measured at 645.25 ± 0.3 nm. The Point Grey GS3 camera was rotated to 6.78° to capture the diffraction pattern. The exposure time of the camera was then set to continuous, and the intensity of the laser was reduced to capture a high-quality image of the diffraction pattern. This process was repeated for all 10 patterns on the sample, then repeated with the sample rotated 90^{o} about the axis perpendicular to the sample plane. Each pattern was imaged again with the addition of the aperture, which was used to ensure that the incident beam covered the

entire pattern. The aperture opening was set to a 1.8 mm diameter. After imaging each pattern with the aperture, a polarized was added to the optical set up in order to investigate the polarization dependence of the pattern. Figure 3.7 shows all 10 of the diffraction patterns printed onto sample 18.

Figure 3.7: The 9 OAM diffraction patterns (1-9) and the annealing control pattern (10) of sample 18.

After capturing images of the first-order Bragg peaks, the half-order diffraction was examined. The half-order Bragg peak was expected at -21.96° using equation 2.4. The aperture was set to a 1.8 mm diameter. The Point Grey GS3 camera was rotated to -21.96° to capture the half-order diffraction. The exposure time of the camera was then set

to continuous to capture the highest quality image of the diffraction pattern. While investigating the half-order diffraction, an off-axis diffraction pattern was observed at the diffraction angle rotated 90° about the sample plane. This image was captured using the Point Grey GS3 camera. The half-order diffraction was also investigated after rotating the sample 90^{o} about the axis perpendicular to the sample plane.

Sample 18 was magnetized using a small permanent magnet to reorder the magnetic structure of the Py. The disappearance of the half-order diffraction was expected and was investigated by looking for a difference in the light detected by the Point Grey GS3 camera at -21.96°. The effect of magnetization on the off-axis diffraction pattern was also investigated. The sample was then heated at 403 K to demagnetize the magnetic structure. The half-order diffraction was expected to return and was investigated using the Point Grey GS3 camera in the same fashion.

3.3 Experimental Parameters Investigated

3.3.1 Optical Parameters (n and k) of Permalloy

The optical parameters of Py are essential in determining the permittivity matrix and the sample thickness of Py. VASE modeling software did not contain a sufficient optical model for Py, so the optical parameters had to be determined experimentally. Investigating the optical properties of Py within a large range of wavelengths (370 to 1000 nm) helps to ensure the correct modeling of the material. Finding the optical parameters is also beneficial because using an ellipsometer to measure thickness is more cost effective and time efficient than using XRR.

3.3.2 Deposition Rates of Permalloy and Aluminum

The deposition rates of Py and Al needed to be determined because the AJA International confocal sputtering system did not have a mechanism to estimate deposition thickness. Deposition time had to be calculated from experimental results in order to accurately create samples with specific thicknesses. The deposition rates in the Hummer Turbo sputtering system did not have to be calculated because it uses a quartz crystal mechanism to estimate deposition thickness.

3.3.3 Voigt Parameter of Permalloy

Because Py is a magneto-optical material, the effects of magnetization should be identifiable using the polarization characteristics of light. These characteristics can be described quantitatively using the Voigt parameter. The Voigt parameter is essential in determining the magneto-optical portion of the permittivity matrix of Py described in Sections 3.3.4 and 4.4. The Voigt parameter was investigated by examining the Kerr rotation and ellipticity of light reflected from Py samples.

3.3.4 Permittivity Matrix of Permalloy

In order to give quantitative meaning to the magneto-optical parameters of Py, it is necessary to identify the value of each element of the permittivity matrix. The permittivity matrix can be calculated using the Voigt parameter and the optical parameters (n and k) of Py

3.3.5 EBL Beam Dose and Accelerating Voltage

The beam dose of the EBL was investigated because it significantly affected the shape and size of each element in the patterned samples. Studying the beam dose was necessary to produce high quality samples. Beam dose is described in equation 3.3. [15]

$$Beam\ dose = \frac{Beam\ Current\ x\ Dwell\ Time}{Step\ Size} \qquad eqn.\ 3.3$$

Beam current is the current of the electron beam, dwell time is time the beam is concentrated in one area, and step size is the distance between successive areas in which the beam is incident. The beam dose was manipulated by changing the beam current within a range of 0.1378 nA to 0.2755 nA. Dwell time and step size were calculated by the EBL software so that a beam current of 0.2755 nA resulted in a beam dose of $110\frac{\mu C}{cm^2}$ when using a 10 kV accelerating voltage, and a beam dose of $330\frac{\mu C}{cm^2}$ when using a 30 kV accelerating voltage.

The accelerating voltage of the EBL was investigated because it affects how electrons interact with the PMMA. Accelerating voltages of 10 kV and 30 kV were studied. Table 3.6 shows the combinations of beam dose, beam current, and accelerating voltages which were investigated. A beam current of 0.2755 nA is considered 100% beam current.

Table 3.6: Combinations of beam dose and accelerating voltage investigated using a 0.2755 nA beam current.

Percent of Maximum Beam Dose (%)	**Accelerating Voltage (kV)**	**Beam Dose** $(\frac{\mu C}{cm^2})$
100	10	110
95	10	104.5
90	10	99
85	10	93.5
80	10	88
75	10	82.5
70	10	77
65	10	71.5
60	10	66
50	10	55
100	30	330
70	30	231

3.3.6 Orbital Angular Momentum (OAM)

Orbital angular momentum was investigated in the diffraction patterns of samples 17 and 18 to determine if the patterns imparted orbital angular momentum on visible light. The investigation of OAM was used to show the validity of the hypothesis presented in Chapter 1.

3.3.7 Magneto-Optical Properties of Permalloy

The half-order Bragg peak was investigated to show that the Py did indeed show magneto-optical properties. The behavior of the half-order diffraction under magnetization and demagnetization was compared.

Chapter 4: Results, Analysis, and Discussion

4.1 Optical Parameters of Permalloy

Three samples consisting of a thin Py film on a Si substrate were scanned using the M-2000 ellipsometer. A dummy layer was created for each sample and the optical (n and k) properties of the Py film were fit to this layer. The optical parameters from each sample were imported into MATLAB where they were averaged and plotted as shown in figure 4.1. These optical properties were then used to calculate the diagonal elements of the permittivity matrix and to create an optical layer model for Py in VASE.

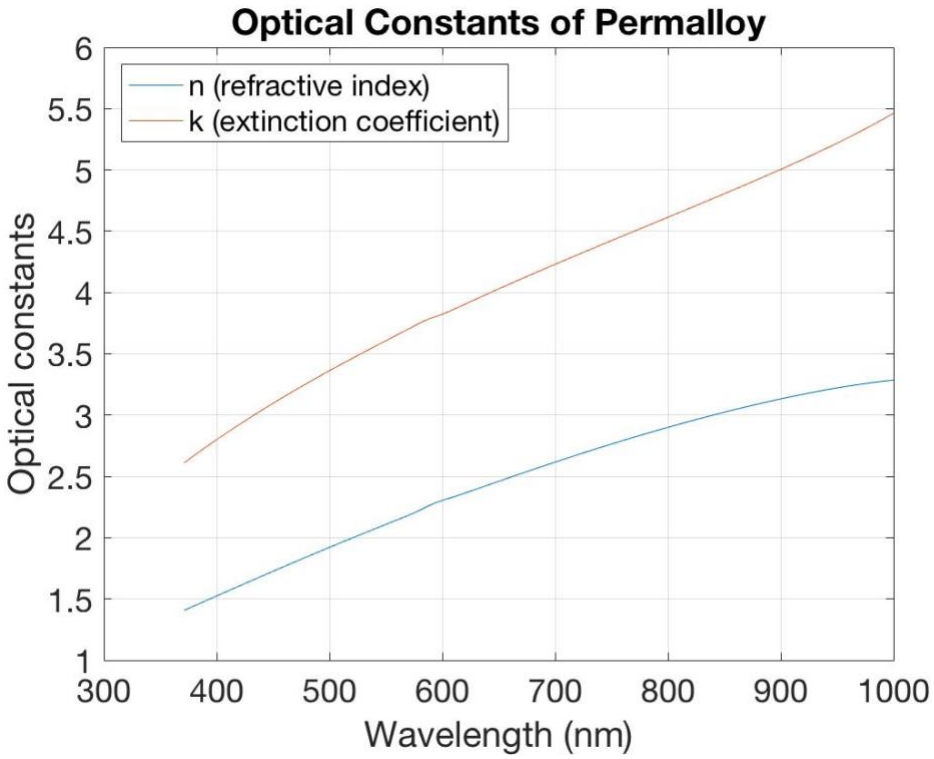

Figure 4.1: The experimentally determined complex n (real) and k (imaginary) optical parameters of Py.

4.2 Deposition Rates of Permalloy and Aluminum

The deposition rates of Py were calculated by using the average thickness measurements from XRR and dividing them by the deposition time. The average Py thickness was 20.4 nm. The time for each deposition was 900 s. The calculated average deposition rate was 0.022 nm/s. The deposition time of a sputter deposition is proportional to the thickness of the deposition considering the plasma conditions remain constant for the entire deposition. [16] Using this deposition rate, specific Py film thicknesses can be deposited in future experiments. The measured thicknesses and calculated deposition rate can be found in table 4.1.

Table 4.1: This table shows the measured Py thickness of each sample, deposition times, and calculated deposition rates. It also shows the average sample thickness and deposition rate.

	Py thickness (nm)	**Deposition Time (s)**	**Deposition rate (nm/s)**
Sample 4	20.9	900	0.023
Sample 5	20.0	900	0.022
Sample 6	20.4	900	0.022
Average	20.4		0.022
Standard Deviation	0.432		0.001

Table 4.2 shows the separate Al and Al_2O_3 measurements with the deposition rates of each Al sample. The measured values for Al deposition in experiments result in an average deposition rate of 0.024 nm/s. Specific Al film thicknesses can be deposited in future experiments using this deposition rate. It should be noted that the total thickness of the Al and Al_2O_3 layers were used to calculate deposition rates. While this may differ

slightly from the actual deposition rate of Al, it is sufficient for the purpose of determining capping layer thickness. Excluding samples 7, 8, 9, and 10, each aluminum film deposition will be approximately 3 nm. At a 3 nm thickness the Al layer is expected to fully oxidize into Al_2O_3. In addition, the Al and Al_2O_3 layer in the experiments performed was only used to prevent the oxidation of the Py layer and does not affect the magneto-optical properties of the samples. Therefore, it is not imperative that the thickness of this layer be exact nor for full oxidation of Al to occur.

Table 4.2: This table shows the measured Al and Al_2O_3 thicknesses of each sample, deposition times, and calculated deposition rates. It also shows the average sample thickness and deposition rate.

	Al thickness (nm)	**Al_2O_3 thickness (nm)**	**Total thickness (nm)**	**Deposition Time (s)**	**Deposition rate (nm/s)**
Sample 7	22.0	8.16	30.1	1200	0.025
Sample 8	9.54	3.80	13.3	507	0.026
Sample 9	8.18	2.59	10.8	507	0.021
Sample 10	8.20	2.63	10.8	507	0.021
Average					0.024
Standard Deviation					0.003

4.3 Voigt Parameter of Permalloy

The Voigt parameter was unable to be positively identified due to limitations with the equipment available for this experiment. The Kerr rotation, Faraday rotation, or the Kerr amplitudes must be identified in order to calculate the Voigt parameter. [17, 18] The Faraday rotation is the change in polarization due to transmission through a medium,

while the Kerr rotation is the change in polarization due to reflection off of a medium. [19] The M-2000, VASE, and Gaertner L117 ellipsometers are unable to measure the Kerr rotation or the Faraday rotation. Ellipsometers equipped to measure the Kerr rotation, or MOKE, utilize a polarizer and analyzer that rotate to find the Kerr rotation for each wavelength during a spectroscopic scan. [17]

Hubert and Schäfer describe a method to calculate the Kerr rotation using equations 4.1 – 4.3. [19] This method was attempted in order to calculate the Kerr rotation of the magnetized samples.

$$A_N = -R_P \cos(\varphi_P) \sin(\alpha_s) + R_s \sin(\varphi_P) \cos(\alpha_s) \qquad \textit{eqn. 4.1}$$

$$A_K = R_K^{pol} \cos(\alpha_s - \varphi_P)\, m_{pol} + R_K^{lon} \cos(\alpha_s + \varphi_P)\, m_{lon} + R_K^{tra} \cos(\varphi_P) \sin(\alpha_s) m_{tra} \qquad \textit{eqn. 4.2}$$

$$\varphi_K = {}^{A_K}/_{A_N} \qquad \textit{eqn. 4.3}$$

In equation 4.1, A_N represents the total signal amplitude relative to the incident amplitude of the light reflected from a magneto-optical material. [19] The reflection coefficients, R_P and R_s, represent the reflection components of the amplitude parallel and perpendicular to the plane of incidence. [19] R_P and R_s are derived from the Fresnel equations for parallel and perpendicularly polarized light. [20] It should be noted that for reflectance (R) and transmittance (T), R + T = 1. R_P, R_s, T_P, and T_s are the reflection and

transmission coefficients, and it is not always true that $R_P + T_P = 1$, or that $R_s + T_s = 1$. [20] The angles of the polarizer and analyzer are given by φ_P and α_s respectively. [19]

In equation 4.2, A_K represents the effective Kerr amplitude of the light reflected from a magneto-optical material. [19] The Kerr amplitudes for the polar, longitudinal and transverse cases are represented by R_K^{pol}, R_K^{lon}, and R_K^{tra} respectively. [19] The magnetization components for the polar, longitudinal, and transverse cases are represented by m_{pol}, m_{lon}, and m_{tra} respectively. [19] The samples magnetized in this experiment were magnetized longitudinally to the point of saturation. The magnetization components in this case become: $m_{pol} = 0$, $m_{lon} = 1$, and $m_{tra} = 0$. Therefore, equation 4.2 simplifies to $A_K = R_K^{lon} \cos(\alpha_s + \varphi_P)$. The Kerr rotation is given by φ_K in equation 4.3.

The Kerr rotation was examined by using the change in polarization measured by the Gaertner L117 ellipsometer, and the reflection and transmission coefficients measured by the M-2000 ellipsometer. The Gaertner ellipsometer was constrained to a wavelength of 632.8 nm so the only data considered from the M-2000 ellipsometer was from a 632.8 nm wavelength. A_N was successfully calculated for multiple samples. A_K was not successfully calculated because of the inability of either ellipsometer to measure R_K^{lon}. The longitudinal Kerr amplitude (R_K^{lon}) can be calculated from equation 4.4, which is dependent on the Voigt parameter, Q. [19]

$$R_K^{lon} = \frac{iQsin\theta_0}{4cos\theta_0 cos\theta_1} T_s T_p \qquad \textit{eqn. 4.4}$$

The transmission coefficients, T_p and T_s, represent the transmission components of the amplitude parallel and perpendicular to the plane of incidence. [19] The angle of incidence, θ_0, was set to 70° in this experiment. The complex angle of incidence, θ_1, is calculated from Snell's Law, $n_0 sin\theta_0 = n_1 sin\theta_1$. [19] In this experiment, $n_0 = 1$ (the refractive index of air), and

$n_1 = n + ik$ (the complex refractive index of permalloy determined in Section 4.1). Rearranging Snell's Law to find θ_1 yields equation 4.5.

$$\theta_1 = sin^{-1}\left(\frac{\sin\theta_0}{n+ik}\right) \qquad \textit{eqn. 4.5}$$

Solving equations 4.1 - 4.5 for the Voigt parameter with a longitudinally magnetically saturated sample yielded equations 4.6 and 4.7. One could calculate the Voigt parameter of the samples used in this experiment with an ellipsometer that measures the Kerr rotation (eqn. 4.6) or the Kerr amplitude (eqn. 4.7). Unfortunately, the ellipsometers used in this experiment could not measure the Kerr rotation, Kerr amplitude, or the transmission coefficients at 70° incidence. A VASE ellipsometer located in the Micro Nano Technology Center at the University of Louisville was used in an attempt to measure the Kerr rotation and Kerr amplitude, but it also lacked the functionality required to measure these parameters. Table 4.3 list the measured values at 632.8 nm for two of the samples in this experiment.

$$Q = \frac{4i\varphi_K(R_P \cos\varphi_P \sin\alpha_s - R_S \sin\varphi_P \cos\alpha_s)\, cos\theta_0 cos\left(sin^{-1}\left(\frac{\sin\theta_0}{n+ik}\right)\right)}{sin\theta_0 T_S T_P} \qquad \textit{eqn. 4.6}$$

$$Q = \frac{-4i\, R_K^{lon} cos\theta_0 cos\left(sin^{-1}\left(\frac{\sin\theta_0}{n+ik}\right)\right)}{sin\theta_0 T_S T_P} \qquad \textit{eqn. 4.7}$$

Table 4.3: Parameters measured for calculating the Voigt parameter at 632.8 nm. Note: R_K^{lon}, T_P, T_s, and φ_K are missing in the table because they were unable to be measured using the equipment available. The N to S orientation expresses a sample where the incident beam originates on the north pole of magnetization, and the reflected beam crosses the south pole of magnetization. In other words, the polarizer is by the north pole of the sample, and the analyzer is by on the south pole of the sample.

	Orientation	$\mathbf{R_P}$	$\mathbf{R_s}$	$\boldsymbol{\varphi_P}$ (º)	$\boldsymbol{\alpha_s}$ (º)	**n**	**k**	$\boldsymbol{\theta_0}$ (º)
Sample 4	N to S	0.308	1.38	71.5	22.7	2.40	3.96	70
	S to N	0.479	1.81	71.4	22.8	2.40	3.96	70
Sample 6	N to S	0.538	1.84	71.2	28.5	2.40	3.96	70
	S to N	0.561	1.89	71.1	28.4	2.40	3.96	70

The Voigt parameter was also investigated using a magneto-optical material model in the VASE software with the M-2000 ellipsometer. The model in VASE fits the Q parameter (Voigt parameter) to an equation input by the user. A quadratic fitting equation using wavelength as the variable was used for the real and imaginary parts of the Voigt parameter. After multiple failed attempts to fit the Voigt parameter, J.A. Woollam was contacted for guidance. The representative from J. A. Woollam advised that the ellipsometers used lacked the sensitivity and precision to measure and fit the Voigt parameter.

Although the Voigt parameter was unable to be described quantitatively, the effects of magnetization are evident in the Δ parameter. The change in the Δ parameter

due to magnetization shows that the magneto-optical effects of Py can be measured using visible light. [18, 19] Figure 4.2 shows the isotropic component of the delta parameter (Δ_E) for sample 6 before and after the magnetic saturation of the sample. The figure also shows the difference of the N-S orientation and S-N orientation measurements of the (Δ_E) parameter. Figure 4.3 shows the ps and sp components (Δ_{ps} and Δ_{sp}) of the Δ parameter for sample 6 before and after the magnetic saturation of the sample. The figure also shows the difference of the N-S orientation and S-N orientation measurements of the ps and sp components of the Δ parameter. Similar results were found in the other magnetically saturated samples: 4, 5, 11, 12, and 13.

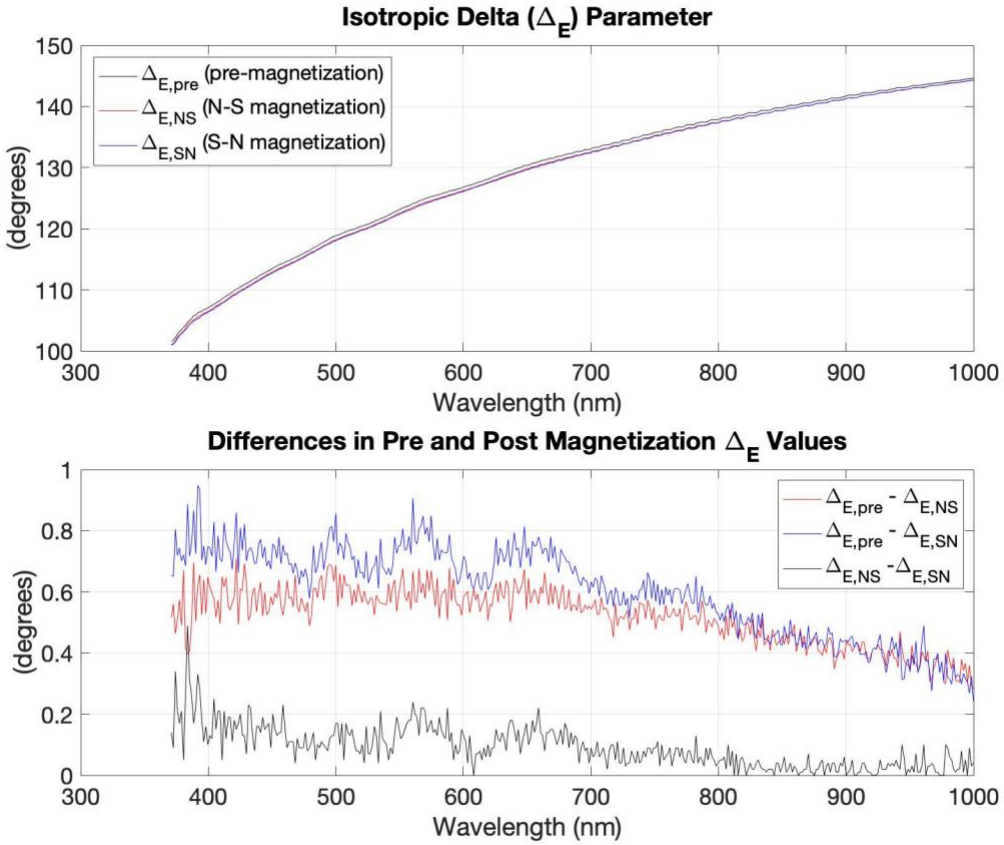

Figure 4.2: The experimentally measured isotropic delta parameter (Δ_E) of sample 6. The top graph shows the sample measured pre-magnetization ($\Delta_{E,pre}$), in a N-S orientation post-magnetization ($\Delta_{E,NS}$), and in a S-N orientation post-magnetization ($\Delta_{E,SN}$). The bottom graph shows the change in the isotropic delta parameter in various configurations.

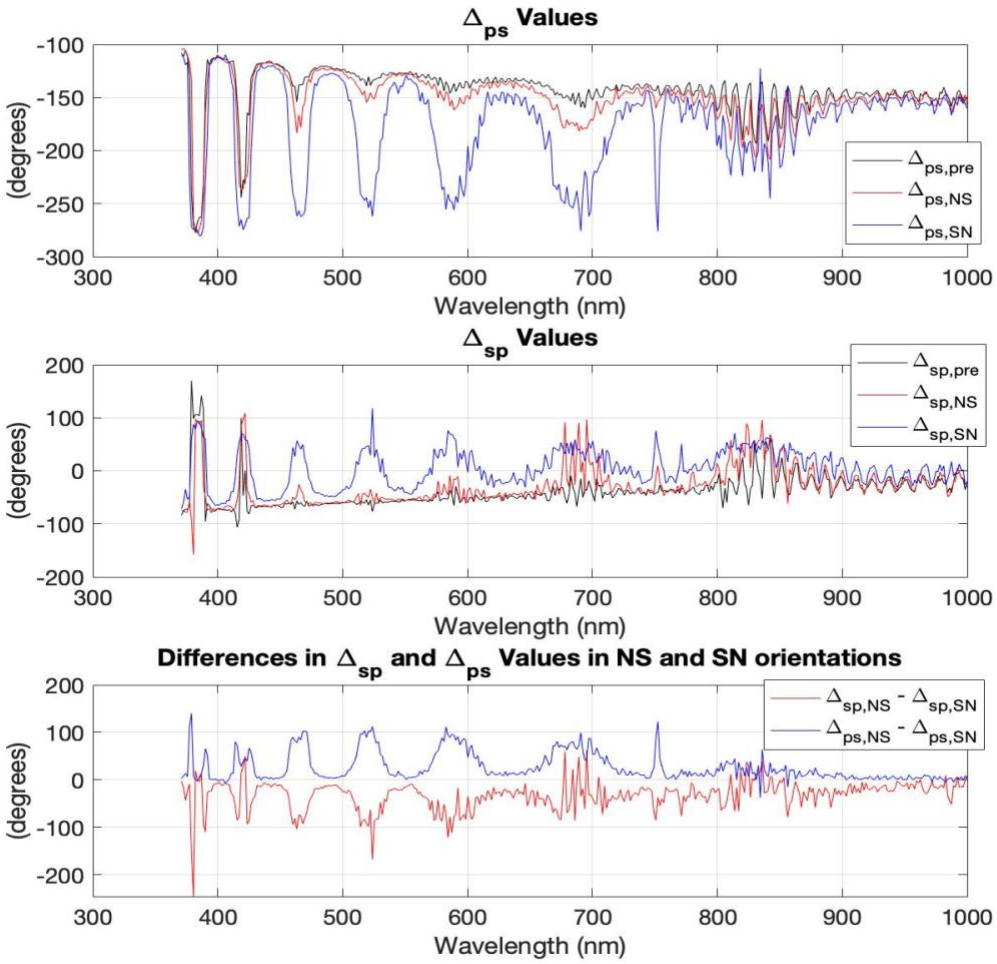

Figure 4.3: The experimentally measured anisotropic delta parameters (Δ_{ps}) *and* (Δ_{sp}) *of sample 6. The top graph shows the* (Δ_{ps}) *parameter of the sample measured pre-magnetization* $(\Delta_{ps,pre})$*, in a N-S orientation post-magnetization* $(\Delta_{ps,NS})$*, and in a S-N orientation post-magnetization* $(\Delta_{ps,SN})$*.. The middle graph shows the* (Δ_{sp}) *parameter of the sample measured pre-magnetization* $(\Delta_{sp,pre})$*, in a N-S orientation post-magnetization* $(\Delta_{sp,NS})$*, and in a S-N orientation post-magnetization* $(\Delta_{sp,SN})$*. The bottom graph shows the differences in N-S and S-N orientations of* (Δ_{ps}) *and* (Δ_{sp}) *parameters.*

4.4 Permittivity Matrix of Permalloy

After determining the complex optical properties n and k, and the Voigt parameter Q, one can calculate the permittivity matrix of Py shown in equation 4.8. [17, 18, 19]

$$\varepsilon = \begin{bmatrix} \varepsilon_{xx} & 0 & 0 \\ 0 & \varepsilon_{xx} & 0 \\ 0 & 0 & \varepsilon_{xx} \end{bmatrix} + iQ \begin{bmatrix} 0 & M_z & -M_y \\ -M_z & 0 & M_x \\ M_y & -M_x & 0 \end{bmatrix} \qquad \textit{eqn. 4.8}$$

In equation 4.8, ε represents the permittivity matrix, ε_{xx} are the field independent elements (independent of magnetization), Q is the Voigt parameter, and $M_{x,y,z}$ are components of the relative magnetization vector. [17] If a sample is magnetically saturated normal to the surface plane, M = (0, 0, 1). [17] Likewise, if a sample is magnetically saturated in plane, M = (1, 1, 0).

The Voigt parameter and the index of refraction contain both real and imaginary parts, where $Q = Q_r + iQ_i$, and $N = n + ik$. [21] The index of refraction is obtained by taking the square of the field independent relativity: $N = \sqrt{\varepsilon_{xx}}$. [19] Furthermore, the permittivity matrix can be expressed as in equation 4.9 by calculating the off-diagonal tensor elements as $\varepsilon_{ij} = iQM_k$, where $i, j, k = x, y, z$. [17] When a sample is magnetically saturated normal to the surface plane, equation 4.9 simplifies to equation 4.10.

$$\varepsilon = \begin{bmatrix} \varepsilon_{xx} & \varepsilon_{xy} & -\varepsilon_{xz} \\ -\varepsilon_{xy} & \varepsilon_{xx} & \varepsilon_{yz} \\ \varepsilon_{xz} & -\varepsilon_{yz} & \varepsilon_{xx} \end{bmatrix} \qquad \textit{eqn. 4.9}$$

$$\varepsilon = \begin{bmatrix} \varepsilon_{xx} & \varepsilon_{xy} & 0 \\ -\varepsilon_{xy} & \varepsilon_{xx} & 0 \\ 0 & 0 & \varepsilon_{xx} \end{bmatrix} \qquad \textit{eqn. 4.10}$$

To calculate ε_{xx}, n and k values were used from the Py model. These values were obtained through calculations based on experimental data from the Py material used in the experiments outlined in Chapter 3. It should be noted that n and k are wavelength dependent. Equations 4.11 – 4.13 were used to calculate ε_{xx}. The real and imaginary parts of ε_{xx} can be seen in figure 4.4. ε_{ij} was unable to be calculated for any i and j combination due to the inability to quantify the Voigt parameter.

$$\varepsilon_{xx} = (n + ik)^2 = n^2 - k^2 + i2nk \qquad \textit{eqn. 4.11}$$

$$\varepsilon_1 = n^2 - k^2 \qquad \textit{eqn. 4.12}$$

$$\varepsilon_2 = i2nk \qquad \textit{eqn. 4.13}$$

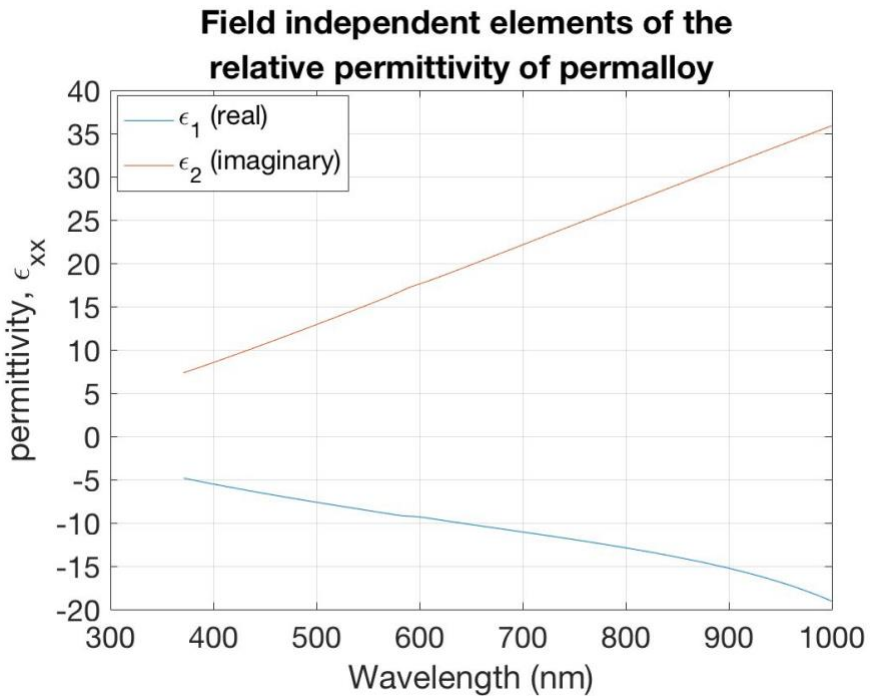

Figure 4.4: This figure shows the real and imaginary parts of the field independent elements of the permittivity matrix, ε_{xx}.

4.5 Effect of Beam Dose and Accelerating Voltage.

The beam dose and accelerating voltage were found to have a large effect on the PMMA, and the overall integrity of the final pattern. The initial accelerating voltage was set to 10 kV and was found to produce a poor-quality pattern with a high beam dose (see figure 4.5 A). The poor-quality pattern is due to the way an EBL works. Electrons are accelerated through an electric field, determined by an accelerating voltage, into the PMMA. The electrons then collide with the PMMA molecules and spread due to forward scattering. [13] The scattering of the electrons exposes the PMMA, changing its molecular chemistry. [13]

Electrons travel slower when using a lower accelerating voltage than they do when using a high accelerating voltage. The reduced speed increases the susceptibility of the electrons to experience collisions with PMMA molecules and other electrons. [13] The increased amount of collisions at lower accelerating voltages cause the electrons to spread out as they travel through the PMMA. Electrons experience forward scattering at higher accelerating voltages as well but experience a lower number of collisions due to increased velocity resulting in a smaller spread of the electron beam. This result of this process is illustrated in figure 4.6.

The degree of the "spread" of electrons when using a 10 kV beam dose was so significant that it caused the pattern in the PMMA to fall apart, as seen in figure 4.5 A. In one sample (referred to as sample 16), nine patterns were created using varying beam doses and a 10 kV accelerating voltage. Upon examination of the patterns created on sample 16, the electron beam did not expose the complete pattern in some cases and caused the pattern to experience damage caused by the forward scattering of electrons in other cases.

The forward scattering of electrons when using a 30 kV accelerating voltage was significantly lower than when using 10 kV. In one sample (referred to as sample 17), two patterns were created using different beam doses and a 30 kV accelerating voltage. Both patterns were successfully created in the PMMA. Figure 4.5 B shows an example of the successful pattern using a 30 kV accelerating voltage where the PMMA maintained adhesion with the substrate.

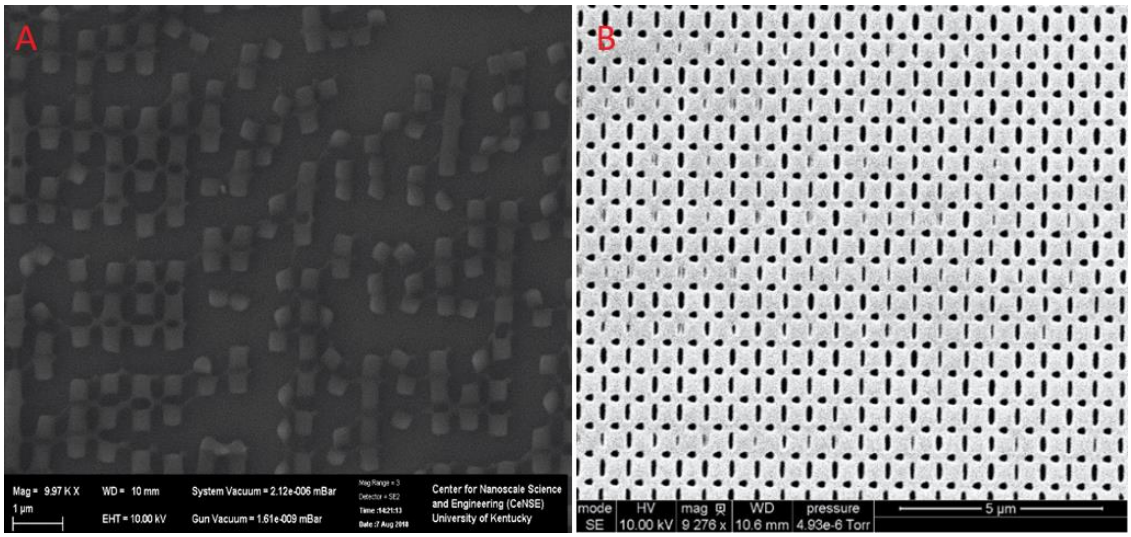

Figure 4.5: A.) The pattern created in the PMMA with a beam dose of 100% (percentage referenced in section 3.3.5 and table 3.6) with an accelerating voltage of 10 kV. B.) The pattern created in the PMMA with a beam dose of 70% with an accelerating voltage of 30 kV. Note: these images were taken with different scanning electron microscopes. The brightness of the PMMA is due to the microscopes used, not the beam dose.

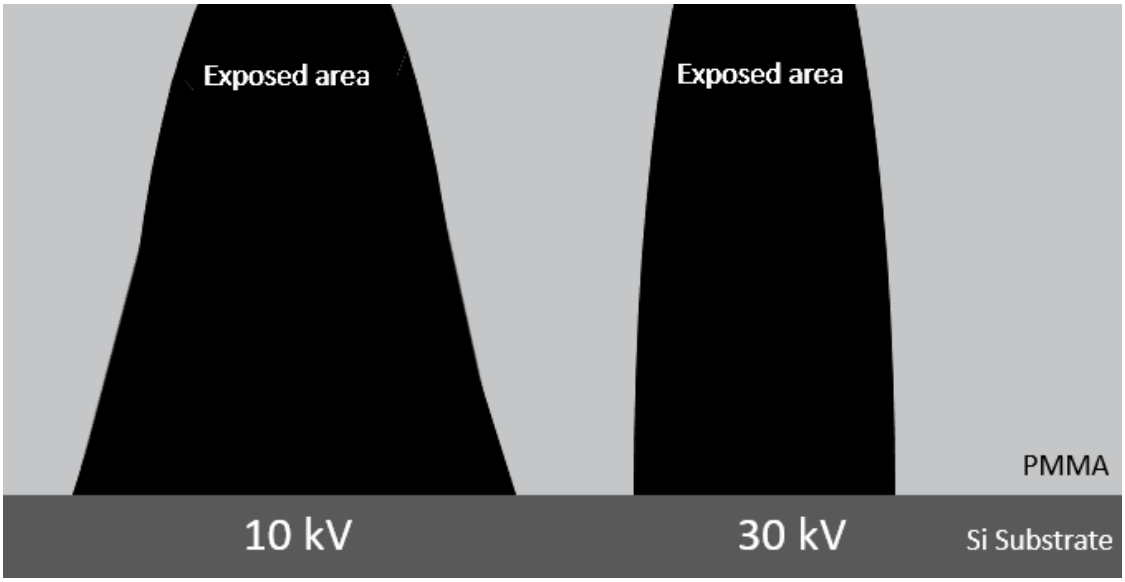

Figure 4.6: The accelerating voltage affects the forward scattering of electrons, changing the exposed area in the PMMA. A 10 kV accelerating voltage causes the electron beam to spread out more as it gets deeper within the PMMA layer than a 30 kV accelerating voltage. This is due to the speed of the electrons as they collide with the PMMA. Note: this cartoon is based on the experimental findings of Mohammad Ali Mohammad et al. [13]

The beam dose affects the shape of the pattern printed into the PMMA. Figure 4.7 shows the patterns printed on sample 17 at 70% and 100% beam doses with a 30 kV accelerating voltage. The 70% dose yields a more uniform and symmetrical pattern. The higher dose yielded a less uniform and symmetrical pattern due to the increased exposure in the PMMA. The 70% beam dose at 30 kV was chosen as the most accurate beam dose for the creation of OAM patterns. It should be noted that the patterns in figure 4.7 are skewed due to errors in the z- stage controller in the Raith EBL. The circle-like shapes as seen in figure 4.7 are meant to be horizontal ellipses, akin to the vertical ellipses in the

pattern. Figure 4.8 shows the final pattern created using a 70% beam dose at 30 kV on sample 17.

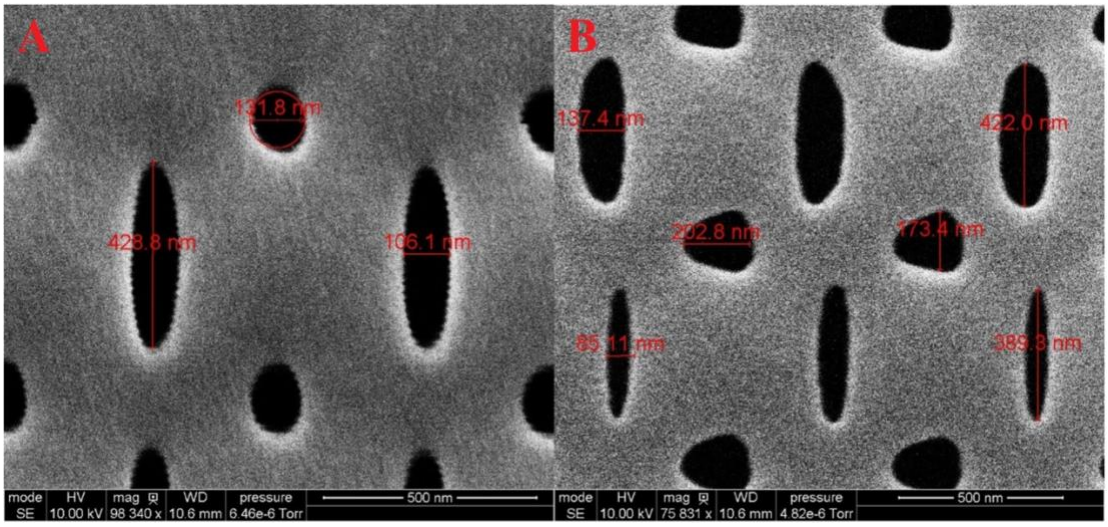

Figure 4.7: A.) This image shows PMMA that was created using a 70% beam dose at 30 kV. B.) This image shows PMMA that was printed using a 100% beam dose at 30 kV. Note: The circles printed should be horizontal ellipses, akin to the vertical ellipses in the pattern.

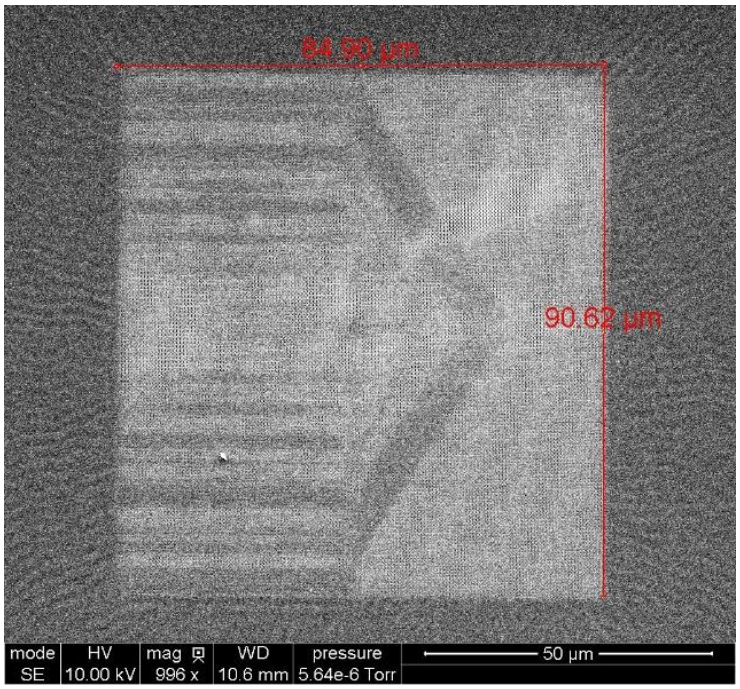

Figure 4.8: The complete pattern created using a 70% beam dose at 30 kV.

4.6 Orbital Angular Momentum

The presence of orbital angular momentum (OAM) was investigated using a 635 nm laser incident on patterned samples. The last sample (sample 17) fabricated at the University of Kentucky was imperfect but was the best sample produced using the Raith EBL. The imperfections in sample 17 are shown in figure 4.9. Sample 17 was not expected to produce any viable results. Interestingly, sample 17 yielded three possible, yet unverifiable, instances of OAM. Figures 4.10 and 4.11 show diffraction patterns that point to the possible presence of OAM in the first-order diffraction Bragg peak from sample 17.

Diffraction patterns 1 and 2 in figure 4.10 are the most promising results from sample 17. Diffraction pattern 1 resembles a horseshoe, or an incomplete ring. This pattern is similar to those found in experiments by Chen at Lawrence Berkley National

Laboratory, using x-ray diffraction. [3] Diffraction pattern 2 appears as a ring of bright light with a dark center and a bright tail. Diffraction pattern 2 resembles a “Q” shape more than the expected “O” shape. Diffraction pattern 2 shows the expected ring of light with a dark center. Diffraction pattern 3 in figure 4.11 was also promising, resembling an elongated “O”. Diffraction pattern 3 is not the brightest peak in the diffraction pattern, which produces doubt that it is caused by OAM. Overall, the results from sample 17 are very interesting but inconclusive.

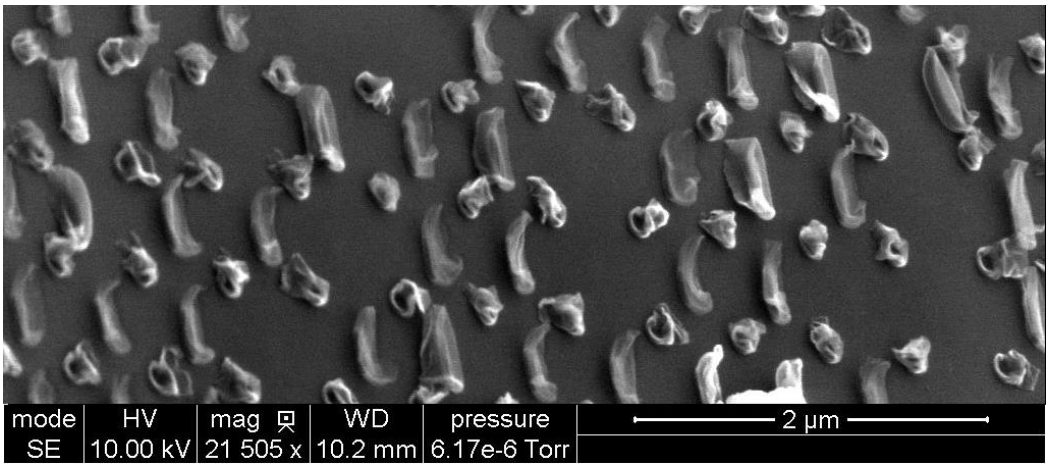

Figure 4.9: The imperfect pattern in sample 17.

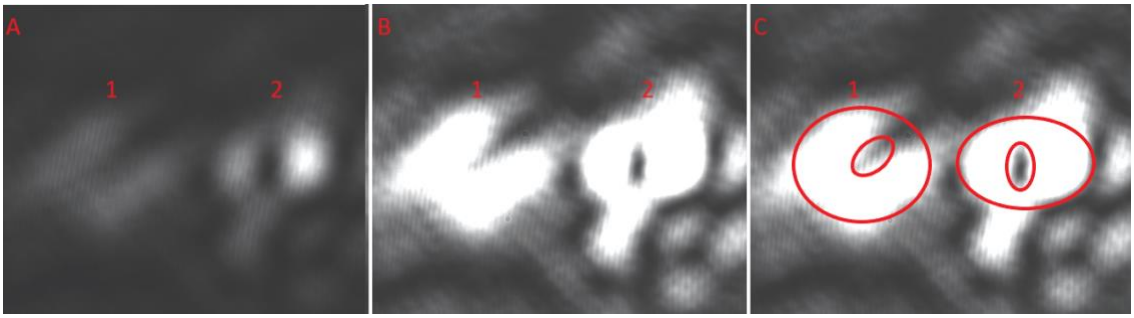

Figure 4.10: This figure shows two of the patterns seen in the first order diffraction of the sample with imperfections. A.) The diffraction patterns without overexposure. B.) The diffraction patterns with high exposure to better show features. C.) The diffraction patterns' possible OAM.

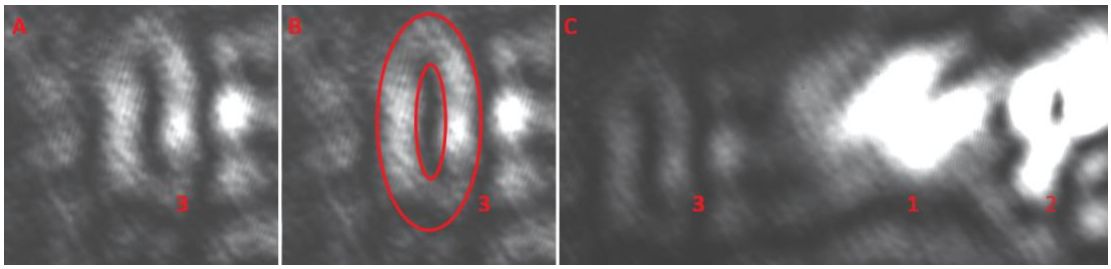

Figure 4.11: This figure shows one of the patterns seen in the first order diffraction of the sample with imperfections. A.) The diffraction pattern without overexposure. B.) The diffraction pattern's possible OAM. C.) The relative location of pattern 3 with patterns 1 and 2.

Sample 18 showed strong evidence of OAM. The images of the diffraction patterns from each OAM pattern on sample 18 without an aperture can be seen in figure 4.12. Diffraction patterns 1-9 resulted in a shape similar to the number "8" with two nulls. Pattern 10 was a standard diffraction pattern and was expected to produce a bright circle with no null, which was observed. Khajavi et al. obtained similar results when

performing an experiment on vortex beam superposition with modes $l = -1$, and $l = -2$. [22] It was noted that while imaging the patterns in figure 4.12, the laser was not centered in the focusing lens. It is possible, though unlikely, that the single mode optical cable used in the experiment was damaged. In this case, the cable could have carried light in the sheath, resulting in a superposition.

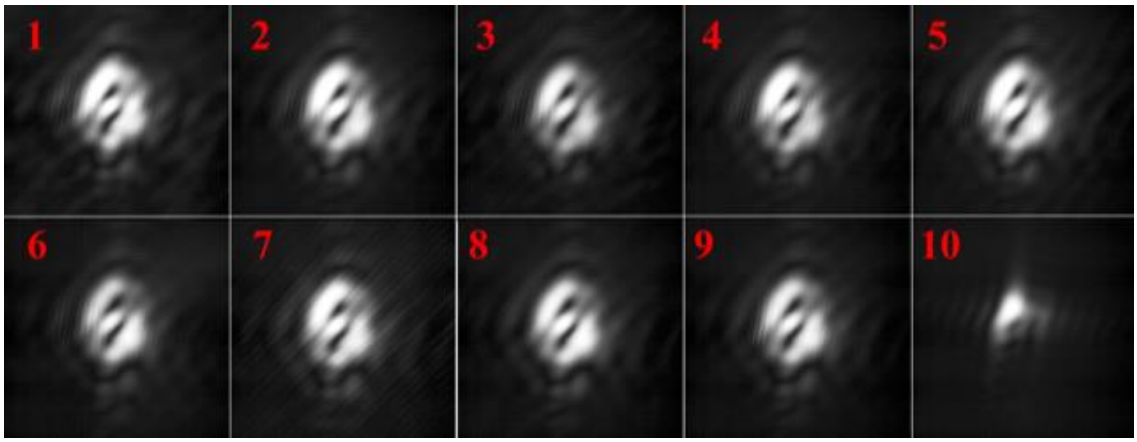

Figure 4.12: This figure shows the diffraction pattern from each OAM diffraction pattern on sample 18 before an aperture was added to the laser. Figure 3.7 shows the location of each pattern on the sample.

The shape of the diffraction patterns produced from sample 18 were extremely sensitive when centering the laser beam. The laser was centered by moving the sample stage with x, y, and z micrometers. Moving the stage more than 2 or 3 μm produced a significant change in the diffraction pattern. It was hypothesized that the beam was too small to cover an entire pattern. A 1.8 mm aperture was added behind the focusing lens in order to spread the beam over an entire pattern. After adding the aperture, the shapes of the diffraction patterns were less sensitive to small movements of the sample stage.

The diffraction patterns were re-imaged after adding the aperture and centering the laser in the focusing lens. The results can be seen in figure 4.13. The resulting patterns resemble a non-canonical edge dislocation OAM pattern as described by Molina-Terriza. [23] Examining the pattern closely revealed two nulls inside of a bright ring. The patterns were reimaged a second time with the aperture and were overexposed with a high contrast. These images are shown in figure 4.14. The overexposed images resemble more typical OAM patterns. [23] The overexposed images were taken to better visualize the bright ring in each diffraction pattern. It should be noted that there are still two nulls present in the overexposed images.

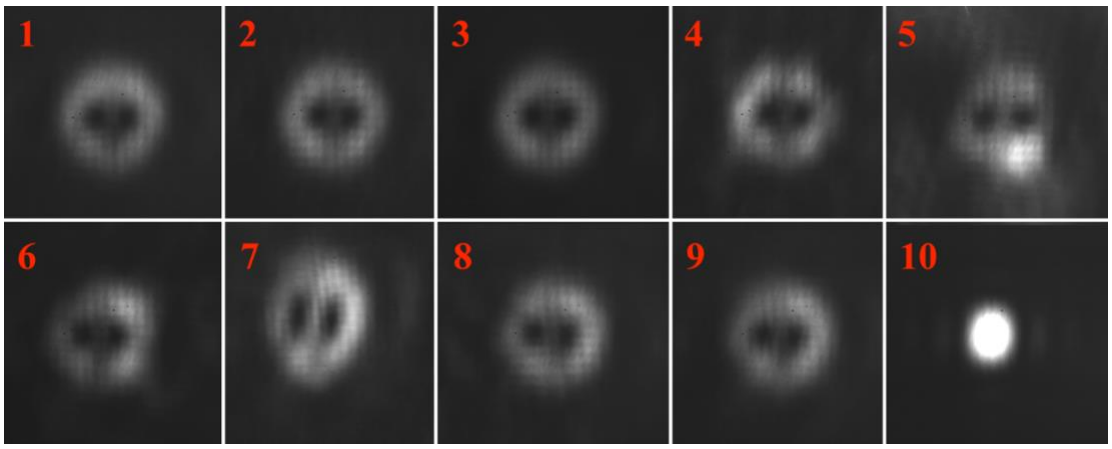

Figure 4.13: This figure shows the diffraction pattern from each OAM diffraction pattern on sample 18 after an aperture was added to the laser. Figure 3.7 shows the location of each pattern on the sample.

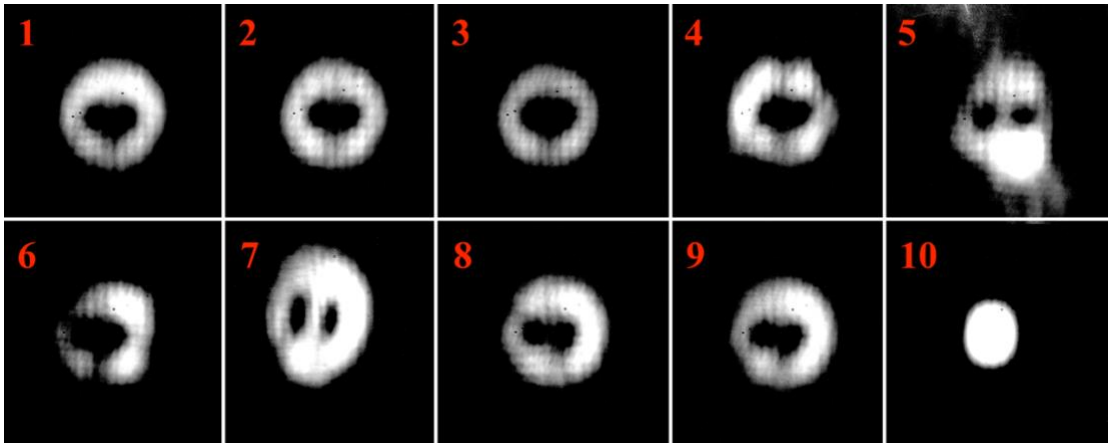

Figure 4.14: This figure shows the diffraction pattern from each OAM diffraction pattern on sample 18 after an aperture was added to the laser. The patterns in this figure were overexposed and imaged with a high contrast. Figure 3.7 shows the location of each pattern on the sample.

A simulation was performed in order to determine the expected diffraction pattern for each OAM pattern. A SEM image of OAM pattern 1 was imported into MATLAB. The pattern was binarized, which is a process that converts each pixel of the image to black or white based on a threshold. The binarization was set so that the background of the image was black, and the OAM pattern was white. The complement of the image was then taken so that the OAM pattern was black on a white background. The Fourier Transform of this image was taken in order to show the diffraction pattern at normal incidence. The simulation was repeated for OAM patterns 2-10. Each step of the simulation process is shown in figures 4.15—4.18. Figure 4.19 shows the first and second-order Bragg peaks of pattern 7 on sample 18. All patterns produced similar results when simulated. It should be noted that the patterns produced by the simulation are at an

incidence of 0°, and the experiment was performed with an incidence of 60°. This may cause the simulated patterns to vary slightly from what is actually expected.

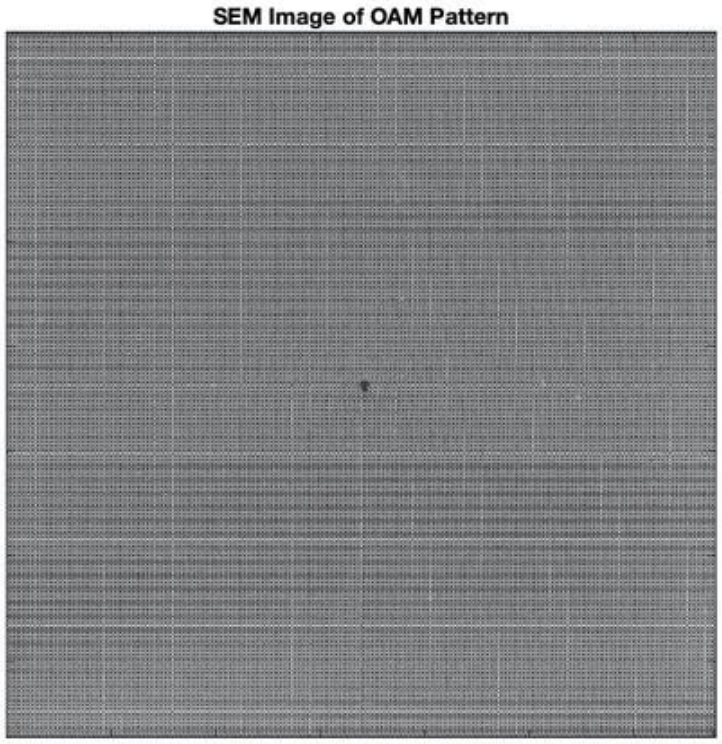

Figure 4.15: The complete SEM image of pattern 7 from sample 18. Note: The elements of this pattern are nanoscale and are not clearly represented in full detail in the figure.

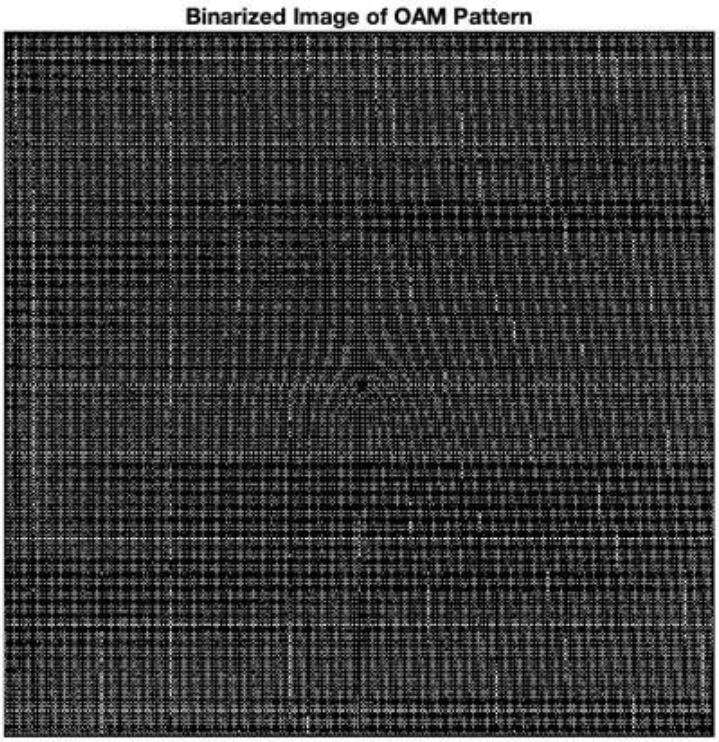

Figure 4.16: The binarized OAM pattern. Note: The elements of this pattern are nanoscale and are not clearly represented in full detail in the figure.

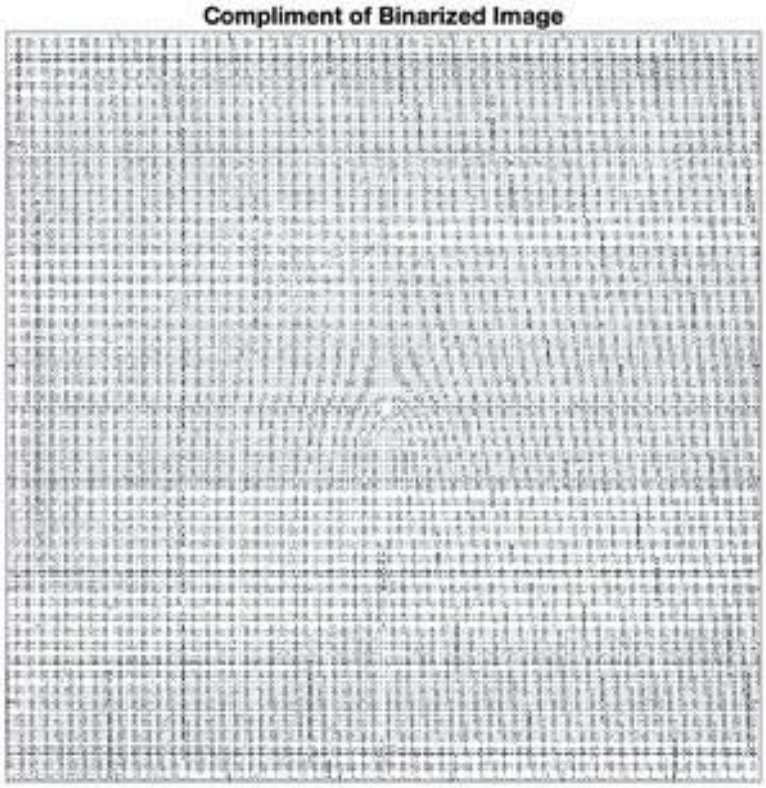

Figure 4.17: The compliment of the binarized image. Note: The elements of this pattern are nanoscale and are not clearly represented in full detail in the figure.

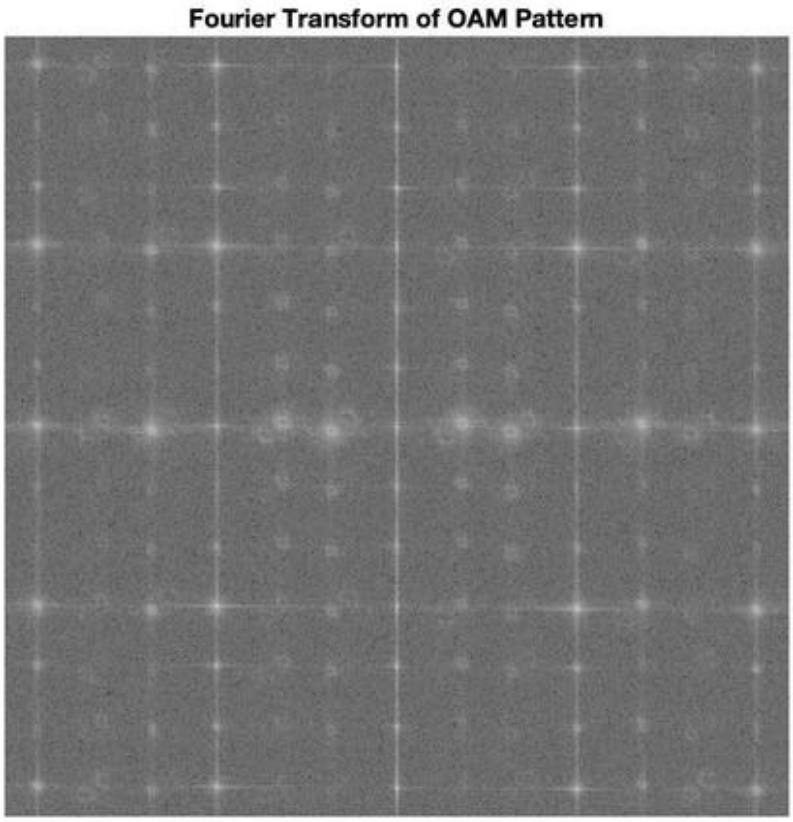

Figure 4.18: The Fourier Transform of the complimented image. The n = (-5, -4, -2, -1, 1, 2, 4, 5) order diffraction patterns appear as two bright rings with a null in the center of each ring.

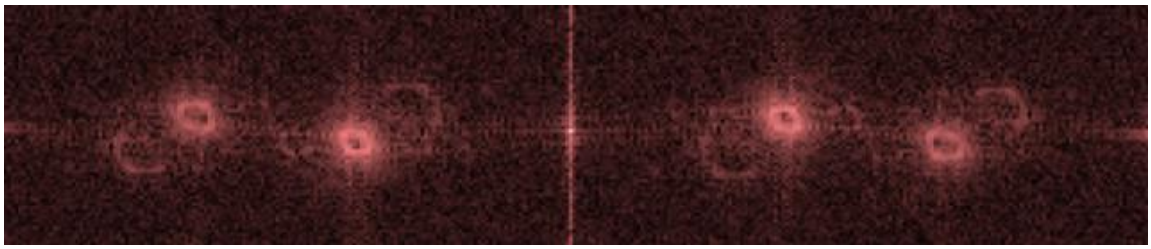

Figure 4.19: A close up of the first and second-order double-ring diffraction pattern simulated from pattern 7. From left to right: n = (-2, -1, 0, -1, 2), where n is the order of the Bragg peak.. Note: A high contrast and red filter were added to the image to make the pattern easier to see.

By examining all of the evidence gathered, the simplest explanation is that the patterns on sample 18 imparted OAM on visible light. The diffraction patterns observed resemble OAM patterns found by Khajavi et al. and described by Molina-Terriza. [22, 23]. A center null was present with a bright ring. The OAM patterns were consistent with the simulated results using a Fourier transform of the patterns, which were designed to impart OAM. The Fourier transform results produced pairs of rings, which was more complicated than expected but consistent with experimental results. More study should be performed to verify these results, such as holography.

4.7 Magneto-Optical Properties of Permalloy

The half-order Bragg peak was investigated using samples 17 and 18. Sample 17 did not display evidence of magnetic scattering in the half-order peak. This is likely due to the imperfect nature of the sample (see figure 4.9). Sample 18 provided interesting

results. Each of the 10 OAM patterns on sample 18 were imaged at the half-order peak. Figure 4.20 shows the images taken where the half-order peak was expected.

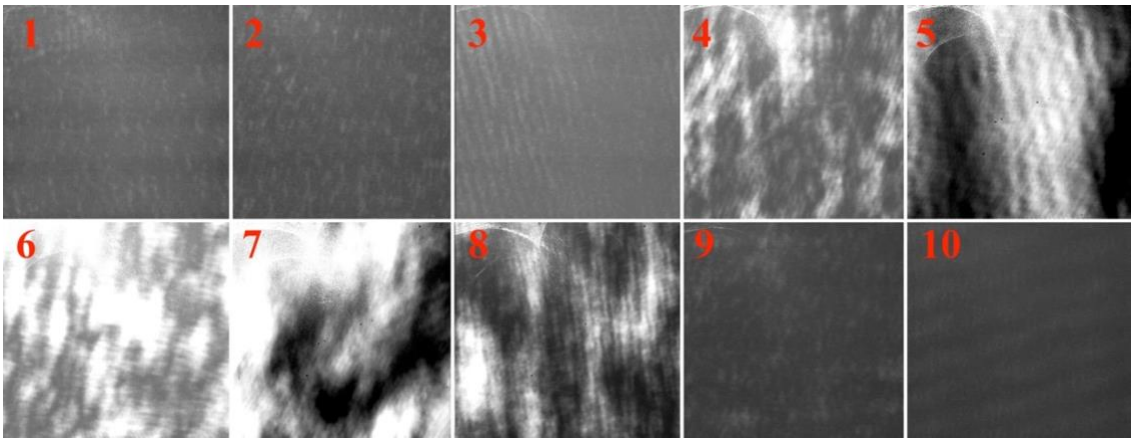

Figure 4.20: The half-order peak of patterns 1-10 on sample 18 show evidence of magnetic scattering. Note: The top left corner of some images shows an artifact due to dust on the camera. Patterns 4, 5, 6, 7 and 8 were found to have been damaged from dust and debris when viewed in a SEM after this experiment.

Each of the 10 OAM patterns showed evidence of magnetic scattering, but the amount of scattering present and the structure of the scattering varied greatly between patterns. Patterns 4, 5, 6, 7, and 8 were found to have been damaged from dust and debris when viewed in a SEM after this experiment. When scattering similar to that in figure 4.20 was observed, sample 18 was heated to 403 K in order to reorder the magnetic domains. It was hypothesized that the sample had been magnetized while in the SEM, and that reordering the magnetic domains would cause the half-order diffraction peak to show an OAM diffraction pattern such as those shown in figures 4.12-4.14. This was not observed.

The magnetic scattering was difficult to distinguish from regular scattering on the sample. In order to verify that the scattering was due to the magneto-optical effects of Py, the sample was magnetized normal to the sample plane. It was hypothesized that magnetizing the sample would reorder the magnetic domains of the sample and that the magnetic scattering in the half-order Bragg peak would no longer be visible once magnetized. This was not observed.

Interestingly, the magnetic scattering in the half order peak changed post-magnetization. This was most noticeable in patterns 3, 4, and 6. In order to determine the cause of the change, the Point Grey GS3 camera was set to record a video. The sample was once again magnetized normal to the sample plane. The camera recorded the half-order peak of pattern 4 for 20 seconds after the magnetization had been removed.

The magnetic scattering changed immediately upon magnetization. Over a period of 2 seconds, the magnetic scattering was observed to change over time. This was repeated multiple times while recording pattern 4 and observed each time. This effect was also recorded using patterns 2, 3, 6, and 7 where it was also observed. Figure 4.21 shows multiple images of pattern 3 in 0.25 second increments post-magnetization to illustrate the change in the magnetic scattering over time. Figure 4.22 shows multiple images of pattern 4 in 0.25 second increments post-magnetization to illustrate the change in the magnetic scattering over time.

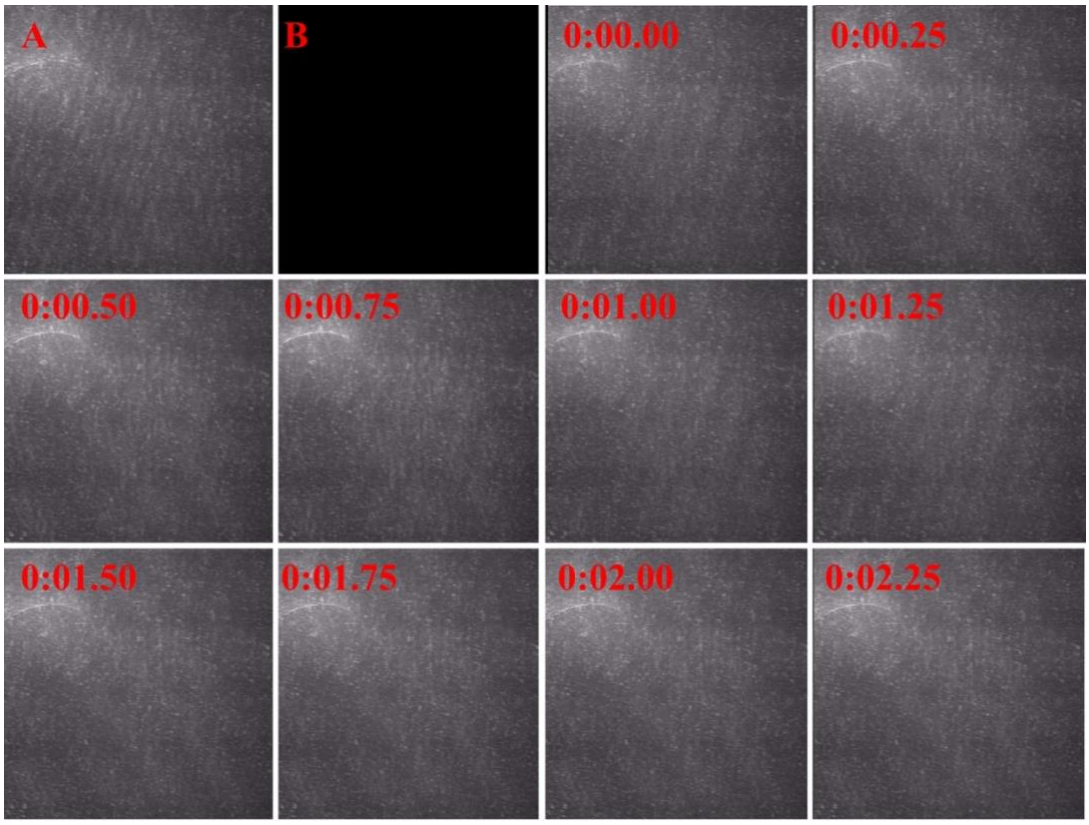

Figure 4.21: The change in the magnetic scattering from pattern 3 on sample 18 over 2 seconds after removing magnetization. The frame marked "A" shows the magnetic scattering pre-magnetization. The frame marked "B" is blank to show a clear separation between pre and post-magnetization. Note: The contrast and brightness were adjusted to better show the features of the magnetic scattering.

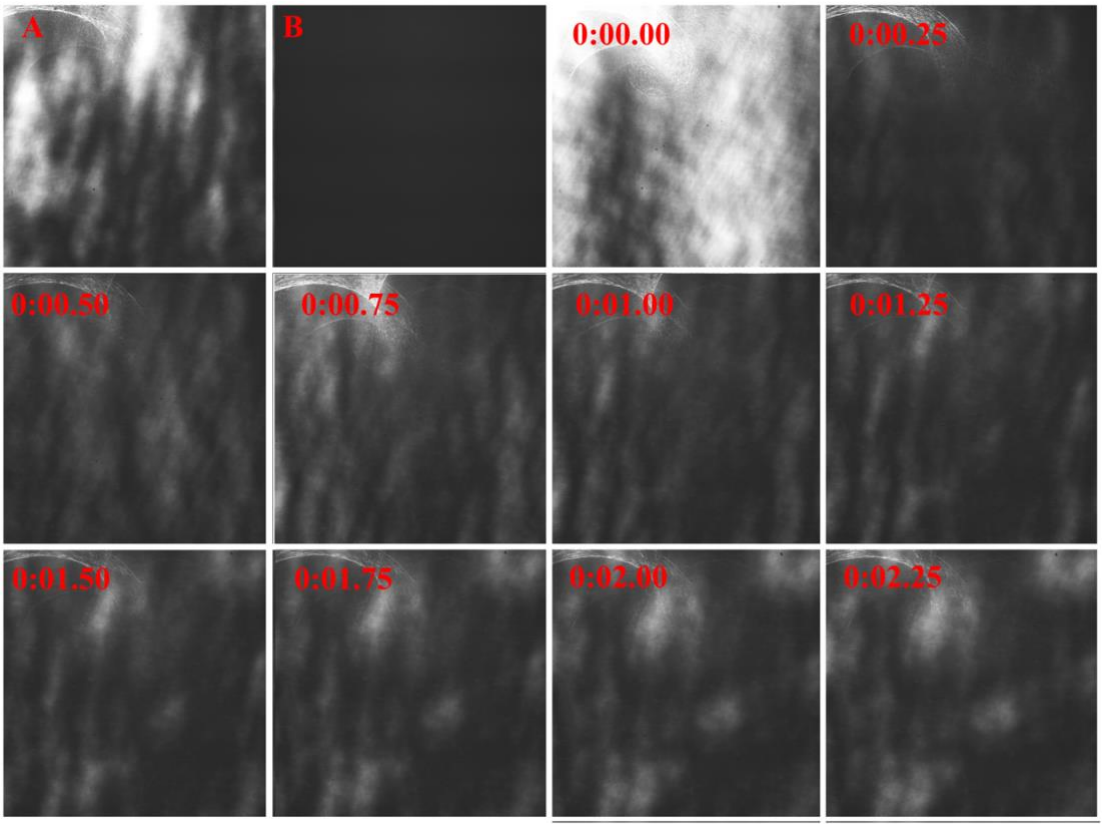

Figure 4.22: The change in the magnetic scattering from pattern 4 on sample 18 over 2 seconds after removing magnetization. The frame marked "A" shows the magnetic scattering pre-magnetization. The frame marked "B" is blank to show a clear separation between pre and post-magnetization.

The magnet used to magnetize the sample when observing the half-order peak had B field of much less than the 0.75 T required to magnetically saturate Py. It is possible that the reordering of the diffraction patterns during magnetization and the subsequent change in the patterns over time post-magnetization could be due to the pattern quickly losing magnetization and returning to the antiferromagnetic ground state. It is also possible that the sample was thermally active enough that the magnetization changed the ASI, but thermal fluctuations were just right to return the sample to an antiferromagnetic

ground state. The possibility that the change in the diffraction pattern is due to a mechanical process, such as the magnet pulling steel springs in the stage, cannot be ruled out. The change in the magnetic scattering at the half-order Bragg peak requires more investigation to reach any conclusions.

Chapter 5: Conclusions

5.1 Future Work

This work provides a foundation for additional study considering the magneto-optical effects of Py on the orbital angular momentum of light. The continuation of this research should include the determination of the Voigt parameter by using ellipsometers designed to measure the MOKE. The Voigt parameter should be used with the index of refraction and extinction coefficient presented in this work to determine the complete permittivity matrix of thin Py. The magneto-optical contributions to diffraction, such as that in the half-order Bragg peak, can be modeled once the complete permittivity matrix of Py has been determined.

The presence of OAM should be definitively confirmed. This can be done using a process such as holography. The complicated multi-null patterns should also be investigated in order to determine the cause of the double-ring shapes seen in this experiment.

The half-order Bragg peak should be examined more closely. It is possible that using a higher intensity laser or more sensitive camera will result in the positive image with and OAM structure in the half-order diffraction. The fluctuations of the magnetic scattering in this experiment due to possible mechanical processes should be confirmed or ruled out.

5.2 Conclusions

In conclusion, the normal part of the permittivity matrix of Py was successfully calculated from the index of refraction and the extinction coefficient measured using spectroscopic ellipsometry. The magneto-optical part of the permittivity matrix was not successfully calculated due to insufficient measurements to accurately calculate the Voigt parameter. However, change in the field-dependent permittivity could be detected by the magnetic-optical effects identified in the Δ parameter of the s and p cross polarizations of non-patterned Py samples. Magnetic scattering at the half-order diffraction peak was observed and showed possible signs of change in the ASI state when magnetized.

The successful creation of patterns consistent with those from a vortex beam in the visible spectrum using a two-dimensional forked magneto-optical diffraction grating was observed. This observation also shows that forked diffraction gratings using square lattice sections generate patterns consistent with OAM. Using forked diffraction gratings with square lattice sections also produces an off-axis diffraction pattern rotated 90^{o} about the sample plane from the incident beam.

After performing more investigation, the shift of the study of the magneto-optical generation of light carrying OAM from the x-ray spectrum to the visible spectrum of light might one day be possible. By using visible light, it is possible to study this phenomenon in a standard lab rather than in a specialized lab using a synchrotron to provide an x-ray beam. This will provide reduced cost, more time in the laboratory with the sample, improve the ease of finding OAM diffraction patterns with the naked eye, and direct access to the sample while imaging. Additional benefits of using the visible light spectrum include studying OAM and magneto-optical effects at shorter timescales using

fast pulse lasers and detectors. [4] Long-term potential includes the fabrication of fast OAM Py modulators for visible light. [4]

References

[1] Zak, J., Moog, E. R., Liu, C., and Bader, S. D., Materials Science Division, Argonne National Laboratory, Argonne, Illinois, "Magneto-optics of multilayers with arbitrary magnetization directions." Physical Review B - Condensed Matter and Materials Physics, vol. 43, no. 8, 1991

[2] MacLyman, William T. "Chapter 2: Magnetic Materials and Their Characteristics." *Transformer and Inductor Design Handbook*. CRC Press, 2011.

[3] Chen, X. M., et al. *Superdomains in Artificial Magnetic Lattices: Fluctuations, Control, and Functionality*. 2018.

[4] Montgomery, Patrick, and J. Todd Hastings. "Personal Communication with J. Todd Hastings, PhD." 2018.

[5] Gutierrez-Vega, J. C. "Chapter 8: Helmholtz-Gauss Beams." *Laster Beam Propagation: Generation and Propagation of Customized Light.* CRC Press, 2014.

[6] Galves, E. J. "Chapter 3: Vector beams in free space." *The Angular Momentum of Light*. Cambridge University Press, 2013.

[7] "What Is Sputtering?" *AJA International*, 2018, www.ajaint.com/what-is-sputtering.html.

[8] LaPuma, Peter, and Martin Zimmerman. "X-Ray Reflectometry." *Good Diffraction Practice Webinar Series*, Brunker. 2010.

[9] Ilic, Bojan (Rob). "Overview." *Woollam - Variable Angle Spectroscopic Ellipsometer*, Cornell Nanoscale Facility, p. 1, 2004.

[10] "What Is Ellipsometry?" *J.A. Woollam*, 2018, www.jawoollam.com/resources/ellipsometry-tutorial/what-is-ellipsometry.

[11] Jesenská, Eva & Hashinaka, Takahiro & Ishibashi, Takayuki & Beran, Lukáš & Dušek, Ján & Antos, Roman & Kuga, Kiyoshi & Aoshima, Ken-ichi & Machida, Kenji & Kinjo,
Hidekazu & Veis, M. "Optical and Magneto-Optical Properties of Gd 22 Fe 78 Thin Films in the Photon Energy Range From 1.5 to 5.5 eV." *Materials*. 2016.

[12] "Ellipsometry Measurements." *J.A. Woollam*, 2018, www.jawoollam.com/resources/ellipsometry-tutorial/ellipsometry-measurements.

[13] Mohammad, Ali, Muhammad, Mustafa, Dew, Steven K., and Stepanova, Maria. Department of Electrical and Computer Engineering, University of Alberta, Edmonton, AB, Canada. “Fundamentals of Electron Beam Exposure and Development.” *Nanofabrication.* Springer-Verlaf/Wein. p.13-16. 2012.

[14] “The Hysteresis Loop and Magnetic Properties.” *Frequency and Pitch*, 2018, www.nde-ed.org/EducationResources/CommunityCollege/MagParticle/Physics/HysteresisLoop.htm

[15] Smith, Gabriel, "Parameters Affecting the Resistivity of LP-EBID Deposited Copper Nanowires". *Theses and Dissertations--Electrical and Computer Engineering.* University of Kentucky, Lexington, KY. 2018.

[16] Montgomery, Patrick, and Amrit Kaphle. “Personal Communication with Amrit Kaphle, PhD Student.” 11 June 2018.

[17] Tikuisis, KK; Beran, L; Cejpek, P; Uhlirova, K; Hamrle, J; Vanatka, M; Urbanek, M; Veis, M, 2017: Optical and Magneto-Optical Properties of Permalloy Thin Films In 0.7-6.4 eV Photon Energy Range. *Materials & Design.* 114, p. 31 – 39. 2016.

[18] Fronk, M., Bräuer, B., Kortus, J., Scmidt, O.G., Zhan, D. R. T., and Salvan, G., “Determination of the Voigt Constant of Phthalocyanines by Magneto-Optical Kerr-Effect Spectroscopy.” *Physical Review B - Condensed Matter and Materials Physics*, vol. 79, no. 23, 2009.

[19] Hubert, A., and Schäfer, R. “Chapter 2: Domain Observation Techniques.” *Magnetic Domains: The Analysis of Magnetic Microstructures*. Springer, 1998.

[20] Mittleman, Daniel M. “Fresnel's Equations for Reflection.” Lecture 13. Brown University. https://www.brown.edu/research/labs/mittleman/sites/brown.edu.research.labs.mittleman/files/uploads/lecture13_0.pdf

[21] Neuber, G., Rauer, R., Kunze, J., Korn, T., Pels, C., Meier, G., Merkt, U., Bäckström, J., and Rübhausen, M. “Temperature-Dependent Spectral Generalized Magneto-Optical Ellipsometry.” *Applied Physics Letters*, vol. 83, no. 22, 2003, pp. 4509–4511. 2003.

[22] Khajavi, B., Gonzales Ureta, J. R., Galvez, E. J., “Determining Vortex-Beam Superpositions by Shear Interferometry.” *hv photonics, MDPI.* 2018.

[23] Molina-Terriza, G. “Chapter 2: Vortex transformations and vortex dynamics in optical fields.” *The Angular Momentum of Light*. Cambridge University Press, 2013.

Vita

Patrick Dean Montgomery

Education:
Certification in Audio Engineering
Lexington School for the Recording Arts, Lexington, KY
GPA: 4.0/4.0

Bachelor of Science in Physics
University of Kentucky, Lexington, KY
GPA: 2.9/4.0

Master of Science in Electrical Engineering
University of Kentucky, Lexington, KY
GPA: 4.0/4.0 (as of December 7, 2018)

Positions Held:
Guitar Center, Assistant Manager (2010-2012)
Long Island Recording Studio, Head of Artist and Repertoire (2012-2013)
YMCA, Aquatics Supervisor (2013-2017)
University of Kentucky, Undergraduate Research/Laboratory Assistant (2015-2017)
University of Kentucky, Graduate Research Assistant (2018)
LG&E and KU Energy, Electrical Engineering Intern III (2017-2018)
LG&E and KU Energy, Electrical Engineer (2018)

Honors:
Member and Officer of Sigma Pi Sigma